

國立臺灣大學生命科學院生化科學研究所



碩士論文

Institute of Biochemical Sciences

College of Life Science

National Taiwan University

Master Thesis

製備活化的 TMPRSS2 胞外域以測試 SARS-CoV-2 進入細胞的抑制劑

Preparation of the activated TMPRSS2 ectodomain for assay of the inhibitors that block SARS-CoV-2 entry

李振維

LI, CHEN-WEI

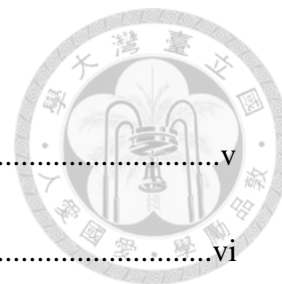
指導教授：梁博煌 博士

Advisor: Po-Huang Liang, Ph.D.


中華民國 112 年 7 月

July 2023

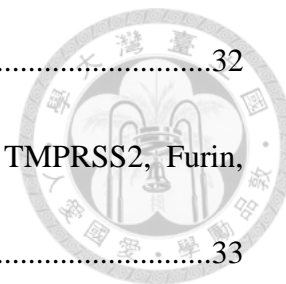
Contents



誌謝	v
中文摘要	vi
Abstract	vii
Abbreviations	viii
1. Introduction	1
2. Materials and Methods	5
2.1. Materials	5
2.2. TMPRSS2 ectodomain expression	5
2.3. TMPRSS2 ectodomain activation and purification	7
2.4. TMPRSS2 kinetics and inhibitory assay	8
2.5. Furin inhibitory assay	9
2.6. Cathepsin L inhibitory assay	10
2.7. Molecular docking	10
3. Results	12
3.1. Purification and characterization of the recombinant TMPRSS2 ectodomain	12
3.2. Test of the synthesized pyrrolidinones for inhibiting TMPRSS2 ectodomain	13

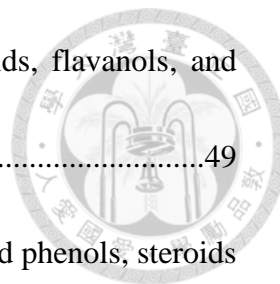


3.3. Binding modes of the pyrrolidinone inhibitors with TMPRSS2	14
3.4. Test of the synthesized pyrrolidinones for inhibiting Furin	15
3.5. Binding modes of the pyrrolidinone inhibitors with Furin	16
3.6. Test of the FDA-approved drugs previously shown to inhibit 3CL ^{pro} and/or PL ^{pro} as antivirals for inhibiting TMPRSS2, Furin, and Cathepsin L	16
3.7. Test of the selected natural products for inhibiting TMPRSS2, Furin, and Cathepsin L	18
3.8. Binding modes of the selected natural products with TMPRSS2	20
3.9. Binding modes of the selected natural products with Furin	21
3.10. Binding modes of the selected natural products with Cathepsin L	21
3.11. Analysis of the selected natural products interacting with the substrate binding pocket of TMPRSS2 or Cathepsin L	22
4. Discussion	23
5. Tables	30
Table 1. Inhibitory effects of compound 2a-l against TMPRSS2, Furin and SARS- CoV-2	30
Table 2. Inhibitory effects of compound 4a-c against TMPRSS2, Furin and SARS- CoV-2	31
Table 3. Inhibitory effects of the FDA-approved drugs against TMPRSS2, Furin,	



Cathepsin L and SARS-CoV-2	32
Table 4. Inhibitory effects of the natural products against TMPRSS2, Furin, Cathepsin L and SARS-CoV-2	33
6. Figures	34
Figure 1. Chemical structures of camostat and nafamostat, and their mechanisms of action for inhibiting TMPRSS2 and virus entry.	34
Figure 2. The subdomains of TMPRSS2 ectodomain and the strategy for the expression of TMPRSS2 ectodomain.	36
Figure 3. Purification of TMPRSS2 ectodomain.	38
Figure 4. Characterization of the kinetic constants of the recombinant TMPRSS2 ectodomain.	40
Figure 5. Inhibition of TMPRSS2 by the synthesized 4-carboxy-1-(4-styryl carbonylphenyl)-2-pyrrolidinones inhibitors.	42
Figure 6. Modeled binding modes of the synthesized pyrrolidinone inhibitor 81 on TMPRSS2 (PDB: 7MEQ).	44
Figure 7. Inhibition of Furin by the synthesized 4-carboxy-1-(4-styryl carbonylphenyl)-2-pyrrolidinones inhibitors.	45
Figure 8. Modeled binding modes of the synthesized pyrrolidinone inhibitor 81 on Furin (PDB: 4RYD).	47

Figure 9. The chemical structures of some selected flavonoids, flavanols, and polyphenols.	49
Figure 10. The chemical structures of some selected unsaturated phenols, steroids with or without sugar moieties, etc.	51
Figure 11. Testing the inhibition of TMPRSS2, Furin, and/or Cathepsin L using the 6 FDA-approved drugs previously been shown to inhibit 3CL ^{pro} and/or PL ^{pro} , as well as antivirals.	53
Figure 12. Inhibition of TMPRSS2 by the selected natural products.	54
Figure 13. Inhibition of Furin by the selected natural products.	56
Figure 14. Inhibition of Cathepsin L by the selected natural products.	57
Figure 15. Modeled binding modes of the selected natural products with TMPRSS2 to rationalize their inhibition specificity.	58
Figure 16. Modeled binding modes of the selected natural products with Furin to rationalize their inhibition specificity.	60
Figure 17. Modeled binding modes of the selected natural products with Cathepsin L to rationalize their inhibition specificity.	62
Figure 18. Analysis of the best inhibitors interacting with the binding pocket of TMPRSS2 or Cathepsin L.	63
7. Reference	65



誌謝




在完成這篇碩士論文之際，我想向所有在這段學術旅程中給予支持、幫助與鼓勵的人們致上最誠摯的謝意。首先，我要感謝我的指導教授-梁博煌博士。感謝您的專業知識、耐心和指導，您在每次進度報告中的建議和指導對我在研究中的成長和進步至關重要。您不僅在學術上指導我，也在生活中給予我許多啟發和支持，讓我能夠克服困難，堅持前行。同樣地，我也衷心感謝我的論文口試委員-徐尚德教授及張淑媛教授。感謝您們在百忙之中抽出寶貴時間閱讀及評估我的論文，並在口試時提出寶貴的意見和建議。您們的寬容與支持使我更深入地理解了我的研究主題，使論文更加完善。

接下來，我要感謝實驗室的同學及學長們，是你們在我做實驗的過程中給予了很多幫助和合作。我收穫了許多珍貴的經驗和友誼，你們的陪伴讓我的研究之旅很有意義。此外，我要感謝我的家人和朋友。感謝你們在我這段學術旅程中的支持和鼓勵，讓我能專心且充實地完成學業。在這個充滿挑戰的學術探索過程中，我收穫了無數寶貴的知識和經驗。這篇論文的完成離不開許多人的幫助，謹向你們致上最真摯的謝意。願這份感激之情永遠存在於我的心中。

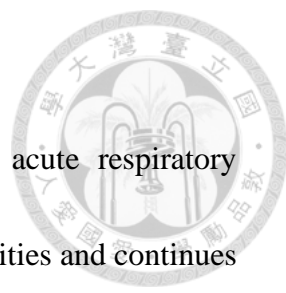
李振維 謹致於國立台灣大學 2023.07

中文摘要



由嚴重急性呼吸道症候群冠狀病毒2型 (SARS-CoV-2) 引起的 2019 年冠狀病毒病 (COVID-19) 已在全球奪去許多人的生命，且仍在蔓延中。病毒在與宿主細胞表面的血管緊張素轉化酶 2 (ACE2) 受體結合後，細胞表面的跨膜絲氨酸蛋白酶 2 (TMPRSS2) 會切割 SARS-CoV-2 刺突蛋白，使病毒與細胞膜融合並進入細胞。因此，已知藥物 (如 camostat 和 nafamostat)，藉著不可逆地抑制 TMPRSS2，從而抑制病毒進入。如本文所述，我使用桿狀病毒感染的昆蟲細胞表達並激活 TMPRSS2 胞外域以測定我們實驗室合成的抑制劑以及選定的天然產物和 FDA 批准的藥物。這些化合物還使用弗林蛋白酶 (Furin) 和組織蛋白酶 L (Cathepsin L) 的試劑進行了分析，Furin 是一種人類細胞表面絲氨酸蛋白酶，可以與 TMPRSS2 分別在刺突蛋白的 S1/S2 及 S2' 位點切割。Cathepsin L 一種參與切割刺突蛋白的細胞內蛋白酶，從而由胞內體釋放入侵的病毒。根據 IC_{50} 建立針對 TMPRSS2、Furin 和/或 Cathepsin L 的抑制劑的構效關係，並通過分子嵌合計算 (docking) 對結構進行模擬以提供抑制的解釋。因此，這項研究提供了可能的 TMPRSS2、Furin 和/或 Cathepsin L 抑制劑來阻止 SARS-CoV-2 進入細胞。

Abstract



Coronavirus disease 2019 (COVID-19), caused by severe acute respiratory syndrome coronavirus 2 (SARS-CoV-2), has resulted in global fatalities and continues to spread. Transmembrane protease, serine 2 (TMPRSS2) on the surface of infected host cells cleaves SARS-CoV-2 spike protein, enabling the primed virus to fuse with the cell membrane and enter the cells after binding with the angiotensin-converting enzyme 2 (ACE2) receptor. Therefore, known antivirals like camostat and nafamostat irreversibly inhibit TMPRSS2 and virus entry. In this thesis, TMPRSS2 ectodomain was expressed using baculovirus-infected insect cells and activated to screen the inhibitors synthesized in our laboratory, as well as the selected natural products and FDA-approved drugs. These compounds were also assayed using the commercial kits to determine their inhibitory effects against Furin and Cathepsin L. Furin is a human cell-surface serine protease that works with TMPRSS2 to cleave the spike protein at the canonical S1/S2 and S2' site, respectively. Cathepsin L is an intracellular protease involved in cleaving the spike protein to release the invading virus from the endosome. Structure-activity relationships of the inhibitors against TMPRSS2, Furin, and/or Cathepsin L were established from the IC_{50} and the complex structures were modeled by the docking program to provide the structural rationale. Therefore, this study offers promising TMPRSS2, Furin, and/or Cathepsin L inhibitors to block SARS-CoV-2 entry.

Abbreviations

CoV, Coronavirus

COVID-19, Coronavirus disease 2019

SARS-CoV-2, Severe acute respiratory syndrome coronavirus 2

TMPRSS2, Transmembrane protease, serine 2

MERS, Middle East respiratory syndrome

SAR, Structure-activity relationship

ACE2, Angiotensin-converting enzyme 2

RBD, Receptor-binding domain

IPTG, Isopropyl β -d-1-thiogalactopyranoside

Ni-NTA, Nickel-nitrilotriacetic acid

3CL^{pro}, 3C-like proteinase

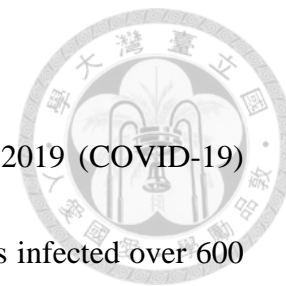
PL^{pro}, Papain-like protease

RdRp, RNA-dependent RNA polymerase

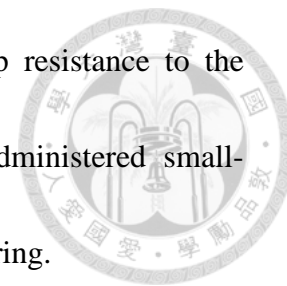


1. Introduction

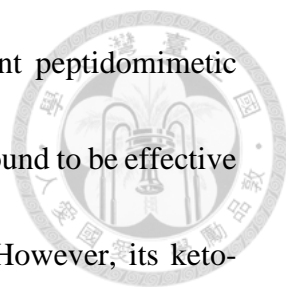
The coronavirus (CoV) disease, first reported in December 2019 (COVID-19) from Wuhan city, China (Zhu et al., 2020; Huang et al., 2020), has infected over 600 million people worldwide and caused the death of more than 6 million patients, with a case fatality rate of approximately 1.1% as of the latest available data. The World Health Organization (WHO) named the causative agent of COVID-19 as SARS-CoV-2 due to its genetic similarity to the virus responsible for the 2002-2003 outbreak, known as SARS-CoV (Peiris et al., 2003; Ksiazek et al., 2003). Both viruses share homology, leading to the identification of the novel virus as SARS-CoV-2. SARS-CoV-2, along with SARS-CoV and MERS-CoV, which caused the previous outbreak starting in Middle Eastern countries in 2012 and spreading to South Korea in 2015 (Zaki et al., 2012; Butler et al., 2012; Cho et al., 2016), all belong to the β subfamily of CoVs (Zhou et al., 2020). The CoVs mentioned above cause an atypical pneumonia infection characterized by a non-productive cough, high fever, and headache. In some cases, the infection can progress to generalized interstitial infiltrates in the human lung. Although three small-molecule drugs, Remdesivir, Molupiravir, and Paxlovid, which inhibit viral replication, as well as therapeutic antibodies against the entry of SARS-CoV-2, have been approved for the treatment of COVID-19 patients, it is still important to explore additional potential drug candidates. This is particularly important due to the potential



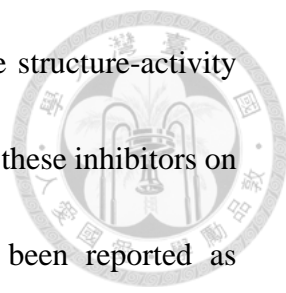
emergence of mutant forms of SARS-CoV-2 that could develop resistance to the currently available drugs. Finding less expensive and orally administered small-molecule drugs to replace expensive antibodies is also worth exploring.



For infection, both SARS-CoV and SARS-CoV-2 utilize human membrane angiotensin-converting enzyme 2 (ACE2) as the anchoring receptor to bind with the virus surface spike glycoprotein through the receptor-binding domain (RBD) of the spike protein. After binding, a human protease Furin cleaves the spike protein into two fragments, S1 and S2, and a transmembrane protease, serine 2 (TMPRSS2) further cleaves S2, enabling the primed virus to fuse with the cell membrane and enter the cells (Bestle D et al., 2020). TMPRSS2 is essential because it can replace the function of Furin. This allows camostat, an irreversible serine protease inhibitor, to antagonize SARS-CoV-2 by inhibiting TMPRSS2 as an off-target (Hoffmann et al., 2020). Nafamostat, which is used as an anticoagulant for disseminated intravascular coagulation and has a structure related to camostat, can also inhibit TMPRSS2 and consequently prevent SARS-CoV-2 infection. The chemical structures of camostat and nafamostat and their mechanisms of inhibiting TMPRSS2 by forming covalent adducts with the protease, are shown in Figure 1A and B, respectively. However, both drugs are potent but non-selective trypsin-like serine protease inhibitors that form a covalent bond with the active-site serine of TMPRSS2 irreversibly (Hoffmann et al., 2020;



Yamamoto M. et al., 2020). A specific ketobenzothiazole covalent peptidomimetic inhibitor, containing a keto warhead and targeting TMPRSS2, was found to be effective against SARS-CoV-2 *in vitro* and *in vivo* (Shapira et al., 2022). However, its keto-reduced hydroxyl reversible inhibitor was unable to inhibit TMPRSS2 and the virus. Therefore, our aim was to develop reversible inhibitors of TMPRSS2 as anti-SARS-CoV-2 agents. Srinivas Palla, a Ph.D. student in our laboratory, synthesized derivatives of pyrrolidinones. Our collaborators, led by Professor Sui-Yuan Chang at the Department of Clinical Laboratory Sciences and Medical Biotechnology, National Taiwan University, have demonstrated that the most effective non-covalent inhibitor in this series could effectively inhibit the delta and omicron strains of SARS-CoV-2. The inhibitor demonstrated a remarkably potent EC_{50} of 2 nM and 6 nM for the delta and omicron strains, respectively. In my work, my objective is to identify enzymes that have the potential to be inhibited by these specific compounds. In addition to the two cell-surface proteases, TMPRSS2 and Furin, the intracellular protease Cathepsin L also plays a crucial role as a target for SARS-CoV-2 entry inhibitors. This is because Cathepsin L is responsible for cleaving the spike protein, releasing the encapsulated virus particle within an endosome, which serves as an alternative pathway for virus entry (Zhao et al., 2021). As reported in this thesis, I prepared TMPRSS2 ectodomain using baculovirus-infected insect cells and purchased the commercial kits of Furin and



Cathepsin L to assay the IC_{50} of the inhibitors and established the structure-activity relationships (SARs) based on computer modeled binding modes of these inhibitors on these proteases. Moreover, the FDA-approved drugs that have been reported as antagonists of SARS-CoV-2 without knowing the exact targets (Kuo et al., 2021), as well as some natural products with structures related to tea polyphenols and some natural products previously demonstrated to inhibit SARS-CoV (Wu et al., 2004; Chen et al., 2005; Wen et al., 2007) were purchased and assayed for inhibiting these proteases. These natural products identified as the proteases inhibitors are being assayed by Professor Chang for their anti-SARS-CoV-2 EC_{50} . From this thesis, several anti-SARS-CoV-2 inhibitors are provided for further development into therapeutic agents for COVID-19.

2. Materials and Methods

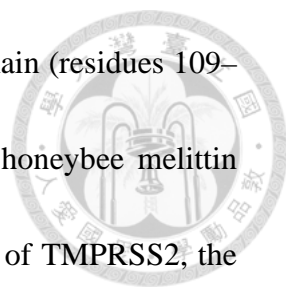


2.1. Materials

The FDA-approved drugs and natural products used in this thesis were purchased from MedChemExpress (NJ, USA) except for Manidipine-2HCl from Adooq Biosciences (CA, USA), Reserpine from ChemFaces (Hubei, China), Epitheafagallin 3-O-gallate from GlpBio (CA, USA), Theaflavin-3-gallate from Cayman Chemical (MI, USA), and Theaflavin-3,3'-digallate from ChromaDex, Inc. (CA, USA). All commercially available reagents used in this study were of the highest grade and were used without any additional purification.

2.2. TMPRSS2 ectodomain expression

Human TMPRSS2 consists of three distinct regions: an intracellular domain, a single-pass transmembrane domain and a biologically active ectodomain. The ectodomain can be further divided into three subdomains: a low-density lipoprotein receptor (LDLR) domain, a scavenger receptor cysteine-rich (SRCR) domain and a C-terminal trypsin-like serine protease (SP) domain, featuring a canonical catalytic triad consisting of H296, D345 and S441. For the expression of TMPRSS2 ectodomain (residues 109–492), a published procedure was followed (Fraser et al., 2022). The gene



was synthesized by BIOTOOLS Co. (Taiwan). TMPRSS2 ectodomain (residues 109–492) was constructed into a pFastbac1 vector with a N-terminal honeybee melittin signal sequence and a C-terminal 8x His tag. To maintain stability of TMPRSS2, the activation sequence SRQSR²⁵⁵ ↓ IVGGE (arrow indicates the cleavage site) on the target protein was replaced with an enterokinase-cleavable DDDDK²⁵⁵ graft with a specific set of primer pairs (5'-gatgatgacgacaagattgtgggctggcgagagc-3'/5'-gttcaagttgaccccgagc-3'), which generated the S251D/R252D/Q253D/S254D/R255K mutations. The plasmid for the expression of TMPRSS2 ectodomain was transformed into *E. coli* DH10Bac cells (Thermo Fisher, catalog no. 10361012, USA) to produce recombinant viral Bacmid DNA.

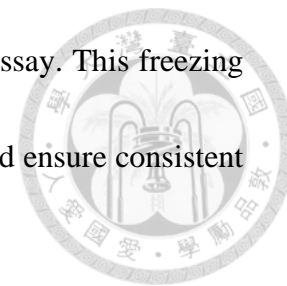
ExpiSf Baculovirus Expression System (Thermo Fisher, catalog no. A38841, A39111, A39112, USA) was utilized to express TMPRSS2 ectodomain at a high level in ExpiSf9 insect cells. ExpiSf9 insect cells were transfected with Bacmid DNA encoding the target protein using ExpiFectamine Sf Transfection Reagent to produce the recombinant baculovirus particles, which were then amplified from P0 to P1 viral stocks. Recombinant P1 virus was used to infect ExpiSf9 insect cells in ExpiSf CD Medium. 2 ml of P1 virus was added per liter of medium after the cell density reached 5×10^6 cells/ml. The cells were then incubated on an orbital shaker (125 r.p.m., 27 °C).

2.3. TMPRSS2 ectodomain activation and purification



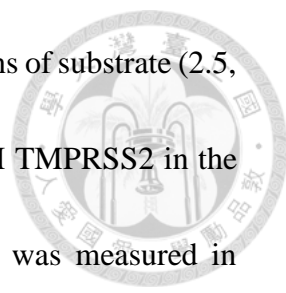
After 4 days of infection (cell viability dropped to 40–50%), cell culture containing the secreted TMPRSS2 ectodomain (residues 109–492)-EFVEHHHHHHHHH was centrifuged (20 min, 10 °C, 6,000 g). The 800 ml of cell-free medium was adjusted to pH7.4 by adding concentrated 10× PBS stock, and was used with a Ni-NTA (HisTrap) column (Cytiva, USA) to capture the target protein. The Ni-NTA (HisTrap) column was washed with 10 column volumes of PBS buffer at pH7.4 with 10 and then 25 mM imidazole and then eluted with 5 column volumes of PBS buffer at pH7.4 with 50, 100 and 250 mM imidazole. The eluted solution was concentrated to 5 mg/ml using 30 kDa MWCO Amicon filters (Merck, Germany). TMPRSS2 ectodomain was activated by adding enterokinase (NEB, USA) at 13 U enzyme per mg and the resulting mixture was then dialyzed against Assay Buffer (25 mM Tris-HCl at pH8.0, 75 mM NaCl, 2 mM CaCl₂) at room temperature overnight. The activated TMPRSS2 sample was exchanged to size-exclusion chromatography buffer (50 mM Tris-HCl at pH7.4, 250 mM NaCl), spun down at 21,000g, and then loaded onto a Superdex 75 10/300 GL column (GE Healthcare, USA). The fractions spanning the dominant peak eluting at 9.74 ml, confirmed by reducing SDS-PAGE, were pooled and concentrated. Aliquots of concentrated stocks (0.19 mg/ml ~4.3 μM) in the buffer (50 mM Tris-HCl at pH7.4, 250 mM NaCl, and 25% glycerol) were rapidly frozen by liquid nitrogen and stored at

-80 °C until they were thawed immediately prior to each enzyme assay. This freezing and thawing process was employed to minimize autoproteolysis and ensure consistent enzyme concentrations for reproducibility.



2.4. TMPRSS2 kinetics and inhibitory assay

TMPRSS2 activity was assayed using a fluorogenic substrate, Boc-Gln-Ala-Arg-AMC (Bachem, catalog no. 4017019, Switzerland), in a microplate reader (BioTek Synergy H1, USA). In 100 µl reaction mixtures on a 96-well plate (Thermo Scientific, USA) containing 1.3 nM TMPRSS2, 10 µM substrate, and various concentrations of inhibitors in the buffer of 20 mM Tris-HCl at pH7.4 with 1% DMSO for dissolving compounds, fluorescence was monitored for 5 mins at excitation/emission of 355/460 nm. IC₅₀ values were determined by preincubating TMPRSS2 with inhibitors at concentrations ranging from approximately half to 5-fold IC₅₀ values for 5 mins. Then, the concentration-dependent TMPRSS2 inhibition curves were fitted with the equation: $A(I) = A(0) \times \{1 - [I / (I + IC_{50})]\}$ using GraphPad Prism (v.9.4.0). In this equation, A(I) is the enzyme activity with inhibitor concentration I, A(0) is the enzyme activity without any inhibitor, and I is the inhibitor concentration. For each data point, the measurements were repeated three times to yield the average number and standard deviation.

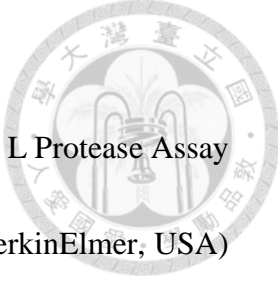


To determine Michaelis-Menten Kinetics, various concentrations of substrate (2.5, 6.25, 12.5, 25, 50, 75, 100, and 150 μM) were reacted with 1.3 nM TMRSS2 in the buffer of 20 mM Tris-HCl at pH7.4. Each reaction velocity (V) was measured in triplicate and plotted against substrate concentration after curve fitting in GraphPad (v.9.4.0).

2.5. Furin inhibitory assay

Furin activity was assayed using a commercial Furin Protease Assay Kit (BPS Bioscience, catalog #78040, USA). In 20 μl reaction mixtures on a 384-well plate (PerkinElmer, USA) containing 0.25 ng/ μl Furin, 2 μM substrate, and various concentrations of inhibitors in Assay Buffer with 1% DMSO for dissolving compounds, fluorescence was monitored for 30 mins at excitation/emission of 380/460 nm. IC_{50} values were determined by preincubating Furin with inhibitors at concentrations ranging from approximately half to 5-fold IC_{50} values for 5 mins. Then, the concentration-dependent Furin inhibition curves were fitted with the equation: $A(I) = A(0) \times \{1 - [I / (I + \text{IC}_{50})]\}$ using GraphPad Prism (v.9.4.0). In this equation, A(I) is the enzyme activity with inhibitor concentration I, A(0) is the enzyme activity without any inhibitor, and I is the inhibitor concentration. For each data point, the measurements were repeated three times to yield the average number and standard deviation.

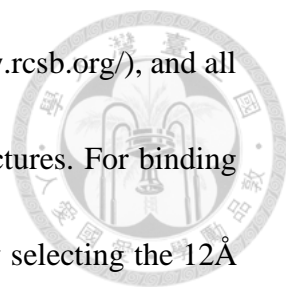
2.6. Cathepsin L inhibitory assay



Cathepsin L activity was assayed using a commercial Cathepsin L Protease Assay Kit (Abcam, UK). In 20 μ l reaction mixtures on a 384-well plate (PerkinElmer, USA) containing the certain concentration of Cathepsin L, substrate, and various concentrations of inhibitors in Assay Buffer with 1% DMSO for dissolving compounds, fluorescence was monitored for 30 mins at excitation/emission of 400/505 nm. IC₅₀ values were determined by preincubating Cathepsin L with inhibitors at concentrations ranging from approximately half to 5-fold IC₅₀ values for 5 mins. Then, the concentration-dependent Furin inhibition curves were fitted with the equation: $A(I) = A(0) \times \{1 - [I / (I + IC_{50})]\}$ using GraphPad Prism (v.9.4.0). In this equation, A(I) is the enzyme activity with inhibitor concentration I, A(0) is the enzyme activity without any inhibitor, and I is the inhibitor concentration. For each data point, the measurements were repeated three times to yield the average number and standard deviation.

2.7. Molecular docking

The molecular docking was performed using the Discovery Studio (DS) 2022 software to predict the binding of compound **81** and natural products with TMPRSS2, Furin, and Cathepsin L. For protein preparation, the three-dimensional (3D) structures of TMPRSS2 (PDB: 7MEQ), Furin (PDB: 4RYD) and Cathepsin L (PDB: 5MQY)



were retrieved from the RCSB protein data bank (PDB, <https://www.rcsb.org/>), and all water molecules and bound ligands were removed from these structures. For binding sites preparation, the binding cavity of TMPRSS2 was extracted by selecting the 12Å radius around the binding site of nafamostat, a known inhibitor of TMPRSS2. Similarly, the binding cavity of Furin was extracted by selecting the 12Å radius around para-guanidinomethyl-Phac-R-Tle-R-Amba, a known Furin inhibitor. The binding cavity of Cathepsin L was also determined, similar to TMPRSS2 and Furin. For ligand preparation, the compound 3D structures of **81** and natural products were generated using the built-in preparation function in DS software. All proteins and ligands were optimized for stable conformation before docking.

Flexible docking is a computational method used in drug discovery to predict how a small molecule drug candidate can bind to a target protein. The method takes into account the flexibility of both the ligand (drug) and the receptor (target protein) during the docking process. All protein-ligand interaction profiles were generated through this docking method, and the different binding interactions were automatically analyzed using DS software. Once the docking process was finished, flexible docking evaluated and ranked all docked poses based on the -CDOCKER Interaction energy (because CDOCKER algorithm is included in flexible docking). As the -CDOCKER Interaction energy increases, the binding affinity between the protein and the ligand was

strengthened, suggesting a more potent and stable molecular interaction.



3. Results

3.1. Purification and characterization of the recombinant TMPRSS2 ectodomain

I followed the reported protocol to express TMPRSS2 ectodomain (residues 109–492), without the transmembrane region (Fraser et al., 2022). The strategy for expressing TMPRSS2 ectodomain and the protocol for activating the expressed TMPRSS2 ectodomain are shown in Figure 2A-C. As mentioned above, the activation sequence SRQSR²⁵⁵ ↓ IVGGE (arrow indicates the cleavage site) located on TMPRSS2 between SRCR and SP domains was replaced with an enterokinase-cleavable DDDDK²⁵⁵ ↓ graft (Fraser et al., 2022). After overexpressing TMPRSS2 ectodomain through baculovirus-infected ExpiSf9 insect cells, the protein was subsequently purified using a Ni-NTA (HisTrap) column. The purified TMPRSS2 was treated with enterokinase to activate TMPRSS2 ectodomain, while SRCR and SP domains remained linked by a disulfide bond.

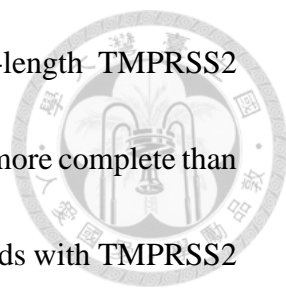
The Ni-NTA purification of TMPRSS2 ectodomain was analyzed by SDS-PAGE, as shown in Figure 3A, including proteins that did not bind to the Ni-NTA (HisTrap) column, labeled as "Ft" (Flow-through), and the target protein eluted using up to 250

mM imidazole. The purified TMPRSS2 ectodomain was activated by enterokinase and further purified using a Superdex 75 10/300 GL column (Figure 3B for SDS-PAGE analysis of the fractions). To confirm the formation of a disulfide bond between SRCR and SP domains, SDS-PAGE was performed under non-reducing and reducing conditions, as shown in Figure 3C.

The purified active TMPRSS2 ectodomain was subjected to kinetic characterization by correlating the fluorescence with the product concentrations using a commercially available BOC-QAR-AMC fluorogenic substrate (Figure 4A and B). The K_m and k_{cat} values were determined by conducting enzymatic assays using 1.3 nM TMPRSS2 and substrate concentrations ranging from 2.5 to 150 μM in 20 mM Tris-HCl buffer at pH7.4. Each well contained a 100 μl reaction mixture. The measured K_m value was $32.3 \pm 9.6 \mu\text{M}$, and the k_{cat} value was $10.5 \pm 1.1 \text{ s}^{-1}$, based on the substrate concentration dependence of the initial velocity profile (Figure 4C).

3.2. Test of the synthesized pyrrolidinones for inhibiting TMPRSS2 ectodomain

Srinivas Palla, a Ph.D. student in our laboratory, synthesized a series of pyrrolidinones (Table 1), which were tested as inhibitors by using the protease domain of TMPRSS2 with a maltose-binding protein (MBP) to enhance solubility in solution

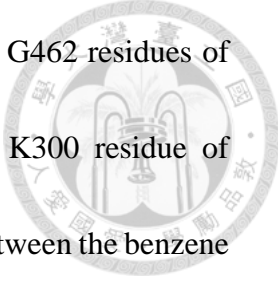


(Kuo et al., unpublished data). Since I prepared the almost full-length TMPRSS2 without the transmembrane domain (TMPRSS2 ectodomain) that is more complete than just the protease domain, I then measured the IC₅₀ of these compounds with TMPRSS2 ectodomain again. As shown in Figure 5, the percentages of inhibition vs. inhibitor concentrations were used to determine the IC₅₀ values for the inhibitors. The best inhibitors, **81** and **143**, showed IC₅₀ of 1.27 ± 0.08 and 3.52 ± 0.55 μM (Table 1), respectively, consistent with the two inhibitors as the most potent antivirals in this series of compounds.

On the other hand, Srinivas also synthesized two compounds, compound **180** and **285** (Table 2), that were similar to compound **100** and **81**, but lacked the carboxylate on the pyrrolidinone. The results showed that they were less potent in inhibiting TMPRSS2 with IC₅₀ of >50 and 31.64 ± 2.93 μM (Figure 5K), respectively.

3.3. Binding modes of the pyrrolidinone inhibitors with TMPRSS2

To elucidate the structure-activity relationship (SAR) of the antivirals in inhibiting TMPRSS2, a docking study was conducted. As shown in Figure 6, our best antiviral so far, **81**, was docked into the active site of TMPRSS2 (PDB: 7MEQ). There were two major binding interactions contributed by the pyrrolidinone, and the indole ring. The



pyrrolidinone formed several hydrogen bonds with S436, S441 and G462 residues of TMPRSS2, while the indole ring formed a hydrogen bond with K300 residue of TMPRSS2 (Figure 6A). In addition, there was a charge interaction between the benzene ring of **81** and H296 residue of TMPRSS2 (Figure 6B). Notably, H296 and S441 are two of TMPRSS2 catalytic triad. This explains why **81** is potent in inhibiting TMPRSS2.

With this binding mode of **81**, other compounds could be evaluated for their binding energies in comparison to that of **81** (not shown). Other compounds with a benzene ring rather than an indole ring, the 3-OH and 4-OH on the benzene ring might form hydrogen bonds with the amino acids and thus bind more tightly. This explains why **103** (R = 4-OH) and **31** (R = 2-fluoro-4-OH) are potential TMPRSS2 inhibitors. However, larger atoms at the 4-position apparently blocked the binding, resulting in less potent inhibition of the enzyme for **22** (R = 4-nitro) and **106** (R = 3,4-dichloro) (Table 1).

3.4. Test of the synthesized pyrrolidinones for inhibiting Furin

I measured the IC₅₀ of these compounds against Furin with the commercial kit. As shown in Figure 7, the percentages of inhibition vs. inhibitor concentrations were used to determine the IC₅₀ values for the inhibitors. The best inhibitors, **81** and **143**, showed IC₅₀ of 3.31 ± 0.52 and 4.55 ± 0.69 μM (Table 1), respectively. In addition, compound

180 and **285** mentioned before also showed less potent in inhibiting Furin. **81** was also tested against Cathepsin L, but no inhibition was found at concentrations up to 50 μM .



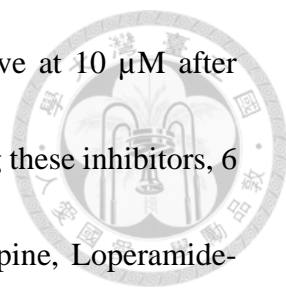
3.5. Binding modes of the pyrrolidinone inhibitors with Furin

Since **81** was the best Furin inhibitors among the tested compounds, I docked **81** into Furin subsequently. As shown in Figure 8, **81** was docked against the Furin protease (PDB: 4RYD). According to the docking results, the pyrrolidinone of **81** formed several hydrogen bonds with R193, H194, R197 and T365 residues of Furin. In addition, the hydrogen of indole group in **81** formed a hydrogen bond with the main chain oxygen of A292 (Figure 8A). Notably, H194 is one of Furin catalytic residues. This explains why **81** is potent in inhibiting Furin.

Furthermore, there were some charge interactions between the carboxyl group of **81** and R193 as well as R197 residues of Furin. And, some hydrophobic interactions were formed between **81** and S253 as well as W254 residues of Furin (Figure 8B).

3.6. Test of the FDA-approved drugs previously shown to inhibit 3CL^{pro} and/or PL^{pro} as antivirals for inhibiting TMPRSS2, Furin, and Cathepsin L

Previously, by screening collections of 1068 and 2701 FDA-approved drugs, we have identified 12 drugs as SARS-CoV-2 3C-like proteinase (3CL^{pro}) inhibitors and 36



drugs as SARS-CoV-2 papain-like protease (PL^{pro}) inhibitors active at 10 μM after excluding any toxic externally used drugs (Kuo et al., 2021). Among these inhibitors, 6 drugs, Proanthocyanidin, Levothyroxine, Manidipine-2HCl, Reserpine, Loperamide-HCl and Maprotiline-HCl, were found to suppress SARS-CoV-2 with EC₅₀ below or close to 10 μM (Kuo et al., 2021). By testing the effectiveness of the screened-out drugs at different stages of virus infection, Proanthocyanidin (EC₅₀ = 2.5 \pm 0.4 μM), Levothyroxine (EC₅₀ = 7.0 \pm 2.2 μM), and Manidipine-2HCl (EC₅₀ = 14.5 \pm 0.8 μM) showed strong antiviral activities at the SARS-CoV-2 entry step. On the other hand, Loperamide-HCl and Maprotiline-HCl inhibited virus replication effectively when applied at the post-entry stage with EC₅₀ of 11.4 \pm 1.6 and 9.3 \pm 0.1 μM , respectively. On the contrast, Reserpine exerted its antiviral activity only when it was treated full-time (entry and post-entry), suggesting that both its PL^{pro}-inhibiting and virus entry-inhibiting activities might contribute to its anti-virus effect (EC₅₀ = 6.6 \pm 1.5 μM). Because Proanthocyanidin, Levothyroxine, Manidipine-2HCl, and Reserpine could inhibit virus entry, I thus measured their anti-TMPRSS2 activities. As shown in Figure 11, only Proanthocyanidin exhibited weak inhibition of TMPRSS2 with IC₅₀ of 47.01 \pm 4.62 μM . Furthermore, these FDA-approved drugs were tested for inhibiting Furin and Cathepsin L. However, none of them showed inhibitory effects at concentrations up to 100 μM (Table 3).

3.7. Test of the selected natural products for inhibiting TMPRSS2, Furin, and Cathepsin L

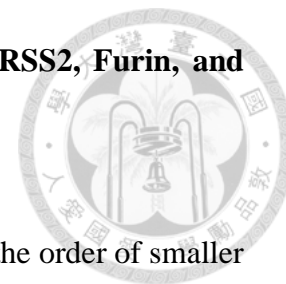


Figure 9 shows the natural products with related structures in the order of smaller to larger sizes, from top-left to bottom-right, including Quercetin, Myricetin, Catechin, Epigallocatechin (EGC), Epicatechin gallate (ECG), Epigallocatechin-3-gallate (EGCG), Theaflavin, Theaflavin-3-gallate, Theaflavin-3'-gallate, Epitheafagallin 3-O-gallate, Theaflavin-3,3'-digallate (TF3), and Proanthocyanidin. The first two compounds, Quercetin and Myricetin, are flavonoids; Catechin is a flavanol; EGC, ECG, or EGCG is a Catechin with an OH, a gallate, or both an OH and a gallate. Theaflavin is a catechin analog fused with a 7-membered ring. Theaflavin-3-gallate, Theaflavin-3'-gallate, and TF3 are theaflavin with a gallate on either side or both sides, respectively. Epitheafagallin 3-O-gallate is similar to Theaflavin-3-gallate but lacks a chromane group. Proanthocyanidin contains two catechin molecules linked with an oxygen. These catechin analogs or catechin-containing molecules were tested in inhibiting TMPRSS2, Furin, and/or Cathepsin L involved in SARS-CoV-2 entry. As shown in Table 4, while Catechin and Quercetin were inactive, Myricetin with an additional OH group compared to Quercetin, inhibited Furin and Cathepsin L with IC_{50} of 24.08 ± 3.52 and 48.21 ± 3.57 μ M, calculated from the dose-dependent inhibition curves as shown in Figure 13A and 14A, respectively. Theaflavin also inhibited

Cathepsin L with IC_{50} of $11.10 \pm 1.14 \mu\text{M}$ (Figure 14B), but the larger Theaflavin-3'-gallate was able to inhibit TMPRSS2, Furin, and Cathepsin L with IC_{50} of 6.21 ± 0.64 , 58.47 ± 6.41 and $51.14 \pm 2.24 \mu\text{M}$ as shown in Figure 12A, 13B and 14C, respectively.

The even larger TF3 exhibited IC_{50} of $5.47 \pm 0.41 \mu\text{M}$ in the inhibition of TMPRSS2 (Figure 12B). In addition, Theaflavin-3-gallate inhibited TMPRSS2 and Furin with IC_{50} of 48.74 ± 3.02 and $36.67 \pm 5.66 \mu\text{M}$ (Figure 12C and Figure 13D), respectively, while Epitheafalagin 3-O-gallate also exhibited IC_{50} of 35.28 ± 2.66 and $55.04 \pm 6.46 \mu\text{M}$ in the inhibition of TMPRSS2 and Furin (Figure 12D and Figure 13C), respectively.

As shown in Figure 10, there are some natural phenol-containing compounds with double bond(s), including some more natural products such as Forskolin and Glycyrrhizic acid. These compounds were recently shown to inhibit the targets for anti-SARS-CoV-2 (Jantan et al., 2022). Additionally, Valinomycin, Escin, and Savinin, which were previously shown by us to inhibit SARS-CoV (Wu et al., 2004; Chen et al., 2005; Wen et al., 2007), are also included. These compounds were purchased to assay their TMPRSS2, Furin, and Cathepsin L inhibiting activities. Among them, only Hispidin showed IC_{50} of $50.11 \pm 3.71 \mu\text{M}$ against TMPRSS2 (Figure 12E).

3.8. Binding modes of the selected natural products with TMPRSS2



According to the TMPRSS2 IC₅₀ data, Theaflavin-3'-gallate and TF3 inhibited TMPRSS2 potently, while Theaflavin could not (Table 4). TMPRSS2 catalytic triad residues are H296, D345 and S441. From the docking result of Theaflavin-3'-gallate, the terminal pyrogallol group could bind to the catalytic pocket of TMPRSS2 and form several hydrogen bonds with C437, G464 and H296 residues of TMPRSS2. The chromane group near the catalytic pocket of TMPRSS2 could also form two hydrogen bonds with G439 and S441 residues of TMPRSS2. (Figure 15A). TF3 could also form several hydrogen bonds with D435, C437 and S441 residues of TMPRSS2 through its chromane group binding to the catalytic pocket of TMPRSS2 (Figure 15B). All results reveal that Theaflavin-3'-gallate and TF3 are potential TMPRSS2 inhibitors.

Theaflavin-3-gallate exhibited a slight inhibition of TMPRSS2 protease activity (Table 4). Compared to the docking result of Theaflavin-3'-gallate, Theaflavin-3-gallate could not form a hydrogen bond with H296, one of TMPRSS2 catalytic triad. This explains why Theaflavin-3-gallate is not as potent as Theaflavin-3'-gallate in inhibiting TMPRSS2.

3.9. Binding modes of the selected natural products with Furin



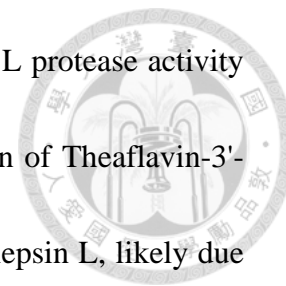
According to the Furin IC_{50} data, we found that the smaller flavonoid-like Myricetin inhibited furin more effectively than the larger ones (Table 4). Furin catalytic residues are D153, H194, N295 and S368. From the docking result of Myricetin, it formed several hydrogen bonds with R197, N295, S363 and S368 residues of Furin (Figure 16A). Theaflavin-3-gallate could form several hydrogen bonds with D154, D191, R193, H194, P256, D258, S363, H364 and T365 residues of Furin (Figure 16B).

Theaflavin-3'-gallate was less potent than Theaflavin-3-gallate in inhibiting Furin (Table 4). Compared to the docking result of Theaflavin-3-gallate, Theaflavin-3'-gallate was unable to form a hydrogen bond with H194, one of Furin catalytic residues (Figure 16C).

3.10. Binding modes of the selected natural products with Cathepsin L

According to the Cathepsin L IC_{50} data, Theaflavin inhibited Cathepsin L potently than any theaflavin analogs I tested (Table 4). Cathepsin L catalytic residues are C25 and H163. From the docking result of Theaflavin, it formed several hydrogen bonds with C25, W26, N66, G68 and H163 residues of Cathepsin L (Figure 17A).

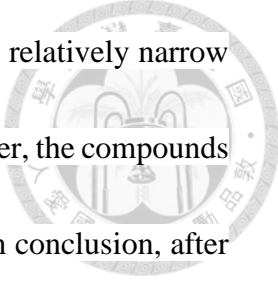
Theaflavin-3'-gallate exhibited a slight inhibition of Cathepsin L protease activity (Table 4). Compared to the docking result of Theaflavin, a portion of Theaflavin-3'-gallate was found to be located outside the active site cleft of Cathepsin L, likely due to the presence of an additional gallate group. As a result, it was unable to form a hydrogen bond with catalytic H163 (Figure 17B).



3.11. Analysis of the selected natural products interacting with the substrate-binding pocket of TMPRSS2 or Cathepsin L

After completing the inhibitory assay of TMPRSS2, Furin and Cathepsin L, I concluded that Theaflavin-3'-gallate and TF3 could inhibit TMPRSS2 potently, while Theaflavin exhibited a strong inhibitory effect against Cathepsin L. Since these compounds have similar but varying sizes of structures, I proceeded to analyze the binding pocket of TMPRSS2 or Cathepsin L that interacted with these natural products.

As shown in Figure 18, both the larger Theaflavin-3'-gallate (Figure 18A) and TF3 (Figure 18B) were located near the S1, S1' and S2 pockets of TMPRSS2, thereby influencing the binding and cleavage of TMPRSS2 substrate. On the other hand, the smaller Theaflavin could occupy the S1 and S2 pockets but not the S1' of Cathepsin L (Figure 18C). This explains why it affects the substrate binding of Cathepsin L.



It is noteworthy that the active cleft of Cathepsin L appears to be relatively narrow and elongated. Therefore, when the chemical structures become bulkier, the compounds may hinder their insertion into the active site cleft of Cathepsin L. In conclusion, after analyzing the IC_{50} and the docking results of Theaflavin and its analogs, we believe the smaller ones are suitable for inhibiting Cathepsin L, while the larger ones are suitable for inhibiting TMPRSS2 among these natural compounds.

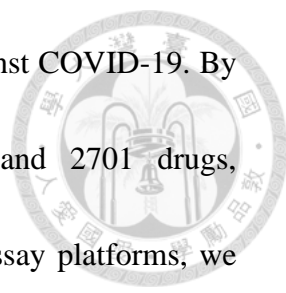
4. Discussion

As demonstrated here, I have expressed and purified the recombinant TMPRSS2 ectodomain, the full-length TMPRSS2 without the transmembrane domain (Figure 2A), measuring its kinetic constants using the AMC-containing substrate Boc-QAR-AMC (Figure 4C). The measured K_m and k_{cat} , which were $32.3 \pm 9.6 \mu M$ and $10.5 \pm 1.1 s^{-1}$, respectively, are consistent with the claim of Fraser's paper (2022). The inhibitors, which were previously synthesized by our laboratory for TMPRSS2 protease domain, were utilized against the recombinant TMPRSS2 ectodomain in this thesis. The best inhibitor **81** showed IC_{50} of $1.27 \pm 0.08 \mu M$ against TMPRSS2 (Table 1). The binding mode of the best inhibitor **81** complexed with TMPRSS2 was simulated, as shown in Figure 6. In the modeled structure, two hydrogen bonds were formed between the

carboxylate group on the pyrrolidinone ring of **81** as well as S436 and G462 residues of TMPRSS2 (Figure 6A). This explains why the absence of the carboxylate results in significantly lower inhibitory activity as comparing compound **81** and its analog **285**.

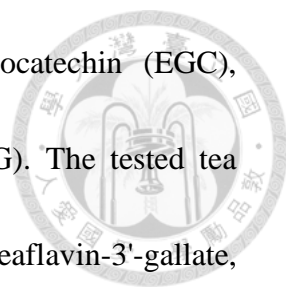
The indole ring of compound **81** also interacted with K300 residue of TMPRSS2.

Because Furin is also involved in priming the spike protein for SARS-CoV-2 entry into cells, their inhibition on Furin was further probed using the commercial assay kit. As summarized in Table 1, **81** is still the best inhibitor against Furin with IC_{50} of $3.31 \pm 0.52 \mu\text{M}$. Computer modeling revealed several hydrogen bonds formed between the pyrrolidinone ring of **81** and R193, H194, R197 and T365 residues of Furin (Figure 8A). These TMPRSS2 and Furin inhibitors have been known for anti-SARS-CoV-2 properties as measured by Professor Sui-Yuan Chang's group, National Taiwan University, but were found only effective during pre-incubation with the virus and during SARS-CoV-2 infection, indicating that their antiviral mechanisms involve inhibiting virus entry. As shown in this thesis, not only **81** but also some analogs have the ability to inhibit TMPRSS2 and Furin, thus preventing the entry of the virus. These compounds are easily synthesized. Since antibodies are quite expensive and small-molecule reversible inhibitors are more suitable as antivirals such as anti-HIV, anti-HCV drugs etc., we thus provide potential candidates to replace therapeutic antibodies for the prevention and/or treatment of COVID-19.



FDA-approved drugs could be used for drug repurposing against COVID-19. By using two FDA-approved drug collections containing 1068 and 2701 drugs, respectively, for screening with SARS-CoV-2 3CL^{pro} and PL^{pro} assay platforms, we identified 6 FDA-approved drugs as active antivirals (Kuo et al., 2021). The further examination of their antiviral mechanisms, 24 drugs exert antiviral activity by blocking virus entry. Therefore, I checked their inhibition on TMPRSS2 and Furin, but only found Proanthocyanidin to exhibit weak inhibition of TMPRSS2 ($IC_{50} = 47.01 \pm 4.62 \mu\text{M}$) (Table 3). Proanthocyanidins belong to a class of polyphenols found in a variety of plants, can function as antioxidants to remove harmful free oxygen radicals from cells, and have been known to confer significant health benefits as reported by several studies using human and animal models (Rauf et al., 2019).

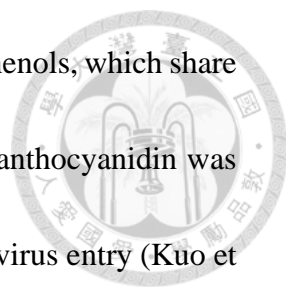
Natural products are known to generally have mild adverse effects, making them potential candidates for the treatment and/or prevention of COVID-19 if they can inhibit SARS-CoV-2. As reported herein, I used TMPRSS2, Furin, and Cathepsin L assays to evaluate the action mechanisms of some selected natural products originally identified with anti-SARS-CoV activities, including some tea polyphenol-related natural products and tea polyphenols (Wu et al., 2004; Chen et al., 2005; Wen et al., 2007). The chemical structures are shown in Figure 9. The examined tea polyphenol-related natural products included flavonoids such as Quercetin and Myricetin, flavanols



such as Catechin, and its gallated analogs, including Epigallocatechin (EGC), Epicatechin gallate (ECG), and Epigallocatechin-3-gallate (EGCG). The tested tea polyphenols included Theaflavin, Theaflavin-3-gallate, Theaflavin-3'-gallate, Epitheafllagallin 3-O-gallate, and TF3, which are antioxidants commonly found in green and black tea, as well as Proanthocyanidin containing two catechin moieties. In these compounds demonstrating inhibition activity, Myricetin, which has the smallest chemical structure, showed moderate anti-Furin activity ($IC_{50} = 24.08 \pm 3.52 \mu M$) and anti-Cathepsin L activity ($IC_{50} = 48.21 \pm 3.57 \mu M$). While Theaflavin displayed promising anti-Cathepsin L activity ($IC_{50} = 11.10 \pm 1.14 \mu M$) and Theaflavin-3'-gallate demonstrated strong inhibition of TMPRSS2 ($IC_{50} = 6.21 \pm 0.64 \mu M$). In addition, TF3, which has the largest chemical structure, potently inhibited TMPRSS2 ($IC_{50} = 5.47 \pm 0.41 \mu M$) (Table 4). Compared to Quercetin, Myricetin containing an additional OH group, displays both Furin and Cathepsin L inhibitory activities. The flavanol analogs of Catechin, EGC, and EGC's gallate adduct, EGCG, are not inhibitors. Theaflavin inhibits Cathepsin L, whereas TF3, which has two additional gallates compared to Theaflavin, inhibits TMPRSS2 instead. Proanthocyanidin with two flavonols also inhibits TMPRSS2, but with less efficiency. From this structure-activity relationship (SAR) analysis, TMPRSS2 has a larger active site compared to Furin and Cathepsin L to accommodate larger inhibitors. Myricetin was reported to antagonize SARS-CoV-2

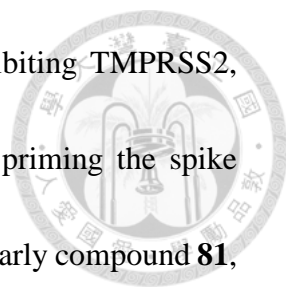
by inhibiting its 3CL^{pro} and ameliorate pulmonary inflammation (Xiao et al., 2021), but they were also found to inhibit RBD:ACE2 interaction and block the entry of pseudovirus (Goc et al., 2021). EGCG and Theaflavin were reported to inhibit 3CL^{pro} of SARS-CoV-2 (Jang et al., 2020), whereas TF3 was predicted to inhibit RNA-dependent RNA polymerase (RdRp) of SARS-CoV-2 (Lung et al., 2020) and antagonize RBD:ACE2 interaction by binding with RBD (Goc et al., 2021).

TF3 is a natural phenol antioxidant found in black tea and has been previously shown to inhibit 3CL^{pro} of SARS-CoV-2 (Chen et al., 2005). As shown in another thesis by Cheng-Chin Lin, it was confirmed that TF3 could inhibit RdRp. However, the inhibitory activity against SARS-CoV-2 came from its inhibition on the virus entry step (Chang, SY et al., unpublished data). Therefore, its RdRp inhibitory activity did not contribute to its antiviral activity. Here, I showed that TF3 could inhibit TMPRSS2 ectodomain, consistent with previous findings that TF3 could inhibit TMPRSS2 protease domain (Kuo et al., unpublished data). Theaflavin-3-gallate, Theaflavin-3'-gallate, and TF3 are the main theaflavins. It is intriguing that Theaflavin can inhibit Cathepsin L, but not TMPRSS2, even though it has similar structure to TF3. Theaflavin could also inhibit virus entry as TF3. Proanthocyanidins, which are oligomeric flavonoids, are a class of polyphenols that can be found in various plants, including cranberry, blueberry, and grape seeds. Many of them are oligomers of catechin and



epicatechin, along with their gallic acid esters. More complex polyphenols, which share the same polymeric building block, form the group of tannins. Proanthocyanidin was shown by us to inhibit 3CL^{pro} of SARS-CoV-2, but it also inhibited virus entry (Kuo et al., 2021). Here, we also demonstrated it could inhibit TMPRSS2 ($IC_{50} = 47.01 \pm 0.62 \mu\text{M}$), which is a target protease for virus entry.

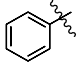
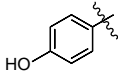
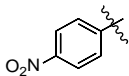
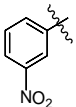
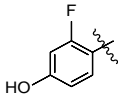
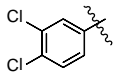
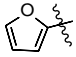
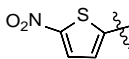
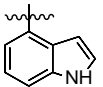
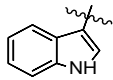
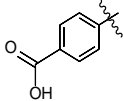
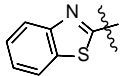
Some other natural products (the chemical structures are shown in Figure 9 and Figure 10) were selected for testing their inhibition on TMPRSS2, Furin, and Cathepsin L. Curcumin was known for its anti-SARS-CoV-2 activity by targeting virus entry from the pseudovirus experiments (Goc et al., 2021) and its properties of immunomodulation and anti-inflammation (Marín-Palma et al., 2021). Quercetin could inhibit RdRp of SARS-CoV-2 for viral replication (Munafo et al., 2022) and SARS-CoV entry into cells (Yi et al., 2004). Glycyrrhizic acid was found to inhibit SARS-CoV-2 by targeting the spike protein and thus RBD:ACE2 interaction (Yu et al., 2021). However, these compounds did not inhibit TMPRSS2, Furin, and Cathepsin L. Valinomycin, Escin, and Savinin have been reported as active inhibitors against SARS-CoV (Chen et al., 2005) and have also inhibited SARS-CoV-2 through post-entry treatment (unpublished data). As expected, they did not inhibit these three human proteases involved in virus entry.



In this thesis, through my assays on the compounds for inhibiting TMPRSS2, Furin, and Cathepsin L, which are human proteases involved in priming the spike protein for SARS-CoV-2 entry, the synthesized compounds, particularly compound **81**, showed more potent dual inhibition of TMPRSS2 and Furin. Additionally, they were found to inhibit the RBD:ACE2 interaction, as probed by Professor Hui-Ching Wang's group from National Tsing Hua University (unpublished results), in cell-based assays. These inhibition activities together led to the potent anti-SARS-CoV activity (**81** reached 2 nM against SARS-CoV-2 delta strain based on plaque reduction assay, measured by Professor Sui-Yuang Chang's group at National Taiwan University). While TF3 and Theaflavin-3'-gallate showed significant TMPRSS2 inhibitory activity, Theaflavin inhibited Cathepsin L. They and some of others also showed potent activity against RBD:ACE2 interaction, as measured by Professor Wang (unpublished results). Therefore, based on this thesis, we provide some reversible SARS-CoV-2 entry inhibitors, which are useful for further development as potential candidates for the prevention and/or treatment of COVID-19.

5. Tables

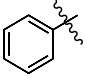
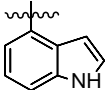
Table 1. Inhibitory effects of compound 2a-l against TMPRSS2, Furin and SARS-CoV-2

Compd	Ar	IC ₅₀ (μM)		EC ₅₀ (μM)	CC ₅₀ (μM)
		TMPrSS2	Furin	SARS-CoV-2	VeroE6
2a (100)		28.35 ± 2.46	23.12 ± 2.35	0.26 ± 0.06 ^a	> 100 ^a
2b (103)		4.32 ± 0.40	4.13 ± 0.41	1.5 ± 0.2 ^a	> 100 ^a
2c (22)		12.46 ± 0.95	10.14 ± 1.12	0.15 ± 0.10 ^a	> 100 ^a
2d (89)		18.20 ± 1.45	18.89 ± 2.30	0.70 ± 0.18 ^a	> 100 ^a
2e (31)		8.02 ± 1.00	8.50 ± 0.57	0.055 ± 0.019 ^a	> 100 ^a
2f (106)		15.81 ± 1.78	16.91 ± 1.83	0.71 ± 0.25 ^a	> 100 ^a
2g (105)		> 50	> 50	1.06 ± 0.54 ^a	> 100 ^a
2h (143)		3.52 ± 0.55	4.55 ± 0.69	0.087 ± 0.010 ^a	59.9 ± 0.99 ^a
2i (81)		1.27 ± 0.08	3.31 ± 0.52	0.002 ± 0.0009 ^a	> 100 ^a
2j (321)		> 50	> 50	No Activity ^a	> 100 ^a
2k (357)		9.99 ± 0.98	10.45 ± 0.67	ND	ND
2l (358)		30.84 ± 3.12	22.66 ± 1.63	ND	ND

^aThe unpublished data were measured by Prof. SY Chang's group.

ND: not determined

Table 2. Inhibitory effects of compound 4a-c against TMPRSS2, Furin and SARS-CoV-2

Compd	Ar	IC ₅₀ (μM)		EC ₅₀ (μM)	CC ₅₀ (μM)
		TMPRSS2	Furin	SARS-CoV-2	VeroE6
4a (180)		> 50	> 50	2.09 ± 0.06 ^a	> 100 ^a
4c (285)		31.64 ± 2.93	> 50	0.67 ± 0.38 ^a	> 100 ^a

^aThe unpublished data were measured by Prof. SY Chang's group.

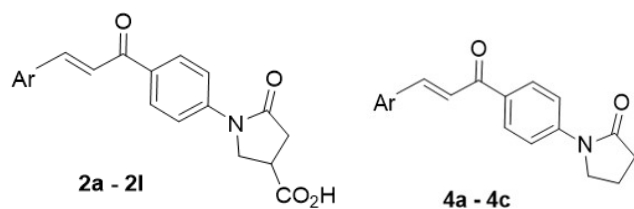
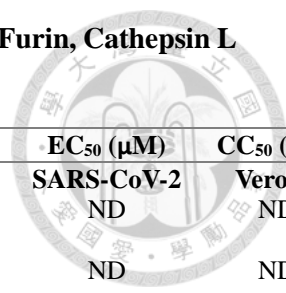


Table 3. Inhibitory effects of the FDA-approved drugs against TMPRSS2, Furin, Cathepsin L and SARS-CoV-2

Compd	IC ₅₀ (μM)			EC ₅₀ (μM)	CC ₅₀ (μM)
	TMPRSS2	Furin	Cathepsin L	SARS-CoV-2	VeroE6
Proanthocyanidin	47.01 ± 4.62	> 100	> 100	2.5 ± 0.4 (entry) ^a	> 100 ^a
Levothyroxine	> 100	> 100	> 100	7.0 ± 2.2 (entry) ^a	> 100 ^a
Manidipine-2HCl	> 100	> 100	> 100	14.5 ± 0.8 (post- entry) ^a	> 100 ^a
Reserpine	> 100	> 100	> 100	6.6 ± 1.5 (entry and post-entry) ^a	> 100 ^a
Loperamide-HCl	> 100	> 100	> 100	33.5 ± 5.8 (post-entry) ^a	56.4 ± 0.7 ^a
Maprotiline-HCl	> 100	> 100	> 100	9.7 ± 0.3 (post-entry) ^a	31.8 ± 0.4 ^a

^aThe data were taken from Kuo et al., 2021.

Table 4. Inhibitory effects of the natural products against TMPRSS2, Furin, Cathepsin L and SARS-CoV-2



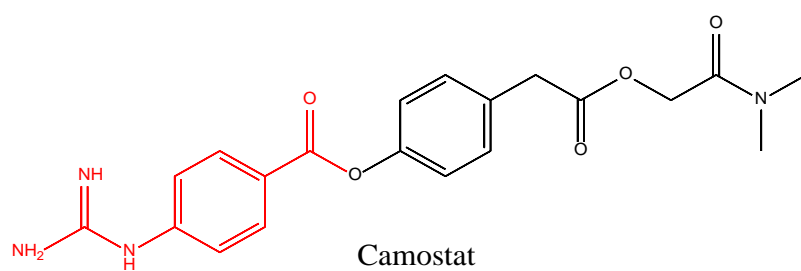
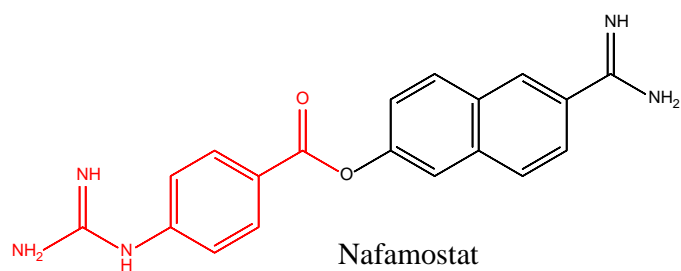
Compd	IC ₅₀ (μM)			EC ₅₀ (μM)	CC ₅₀ (μM)
	TMPRSS2	Furin	Cathepsin L	SARS-CoV-2	VeroE6
Quercetin	> 100	> 100	> 100	ND	ND
Myricetin	> 100	24.08 ± 3.52	48.21 ± 3.57	ND	ND
Catechin	> 100	> 100	> 100	ND	ND
Epigallocatechin (EGC)	> 100	> 100	> 100	ND	ND
Epicatechin gallate (ECG)	> 100	> 100	> 100	ND	ND
Epigallocatechin-3-gallate (EGCG)	> 100	> 100	> 100	ND	ND
Theaflavin	> 100	> 100	11.10 ± 1.14	ND	ND
Theaflavin-3-gallate	48.74 ± 3.02	36.67 ± 5.66	> 100	ND	ND
Theaflavin-3'-gallate	6.21 ± 0.64	58.47 ± 6.41	51.14 ± 2.24	ND	ND
Epitheafllagallin 3-O-gallate	35.28 ± 2.66	55.04 ± 6.46	> 100	ND	ND
Theaflavin-3,3'-digallate (TF3)	5.47 ± 0.41	> 100	> 100	ND	ND
Curcumin	> 100	> 100	Interference	ND	ND
Resveratrol	> 100	> 100	> 100	ND	ND
Hispidin	50.11 ± 3.71	> 100	> 100	ND	ND
Cardamonin	> 100	> 100	> 100	ND	ND
Magnolol	> 100	> 100	> 100	ND	ND
Rosmarinic acid	> 100	> 100	> 100	ND	ND
Betulinic acid	> 100	> 100	> 100	ND	ND
Oleanolic acid	> 100	> 100	> 100	ND	ND
Retinoic acid	> 100	> 100	> 100	ND	ND
Forskolin	> 100	> 100	> 100	ND	ND
Savinin	> 100	> 100	> 100	ND	ND
Glycyrrhizic acid	> 100	> 100	> 100	ND	ND
Escin	> 100	> 100	> 100	ND	ND
Berbamine	> 100	> 100	> 100	ND	ND
Valinomycin	> 100	> 100	> 100	ND	ND

ND: not determined

6. Figures



A



B

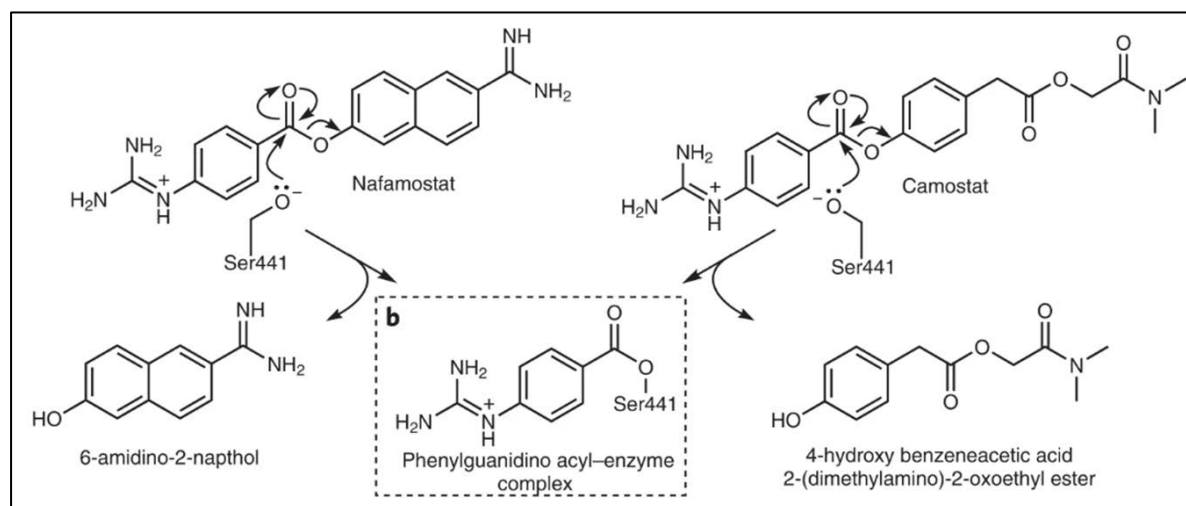
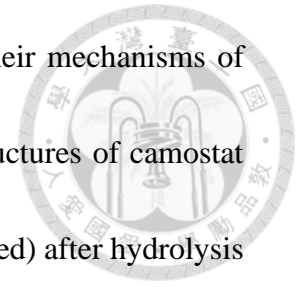
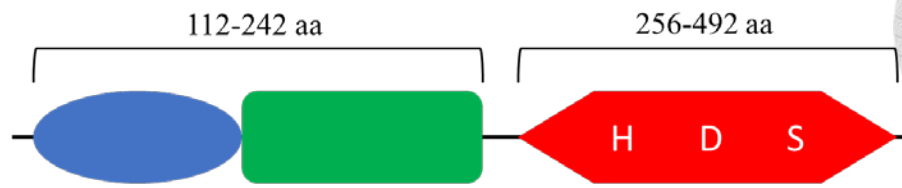




Figure 1. Chemical structures of camostat and nafamostat, and their mechanisms of action for inhibiting TMPRSS2 and virus entry. (A) Chemical structures of camostat and nafamostat. Both have the same leaving group (highlighted in red) after hydrolysis by TMPRSS2. (B) The action mechanisms of camostat and nafamostat for inhibiting TMPRSS2 by forming a covalent bond with the active-site S441 residue. Inhibition of TMPRSS2 should block SARS-CoV-2 entry into cells because cleavage of the viral spike protein by TMPRSS2 is required for entering host cells. The figure is taken from Fraser et al., 2022.

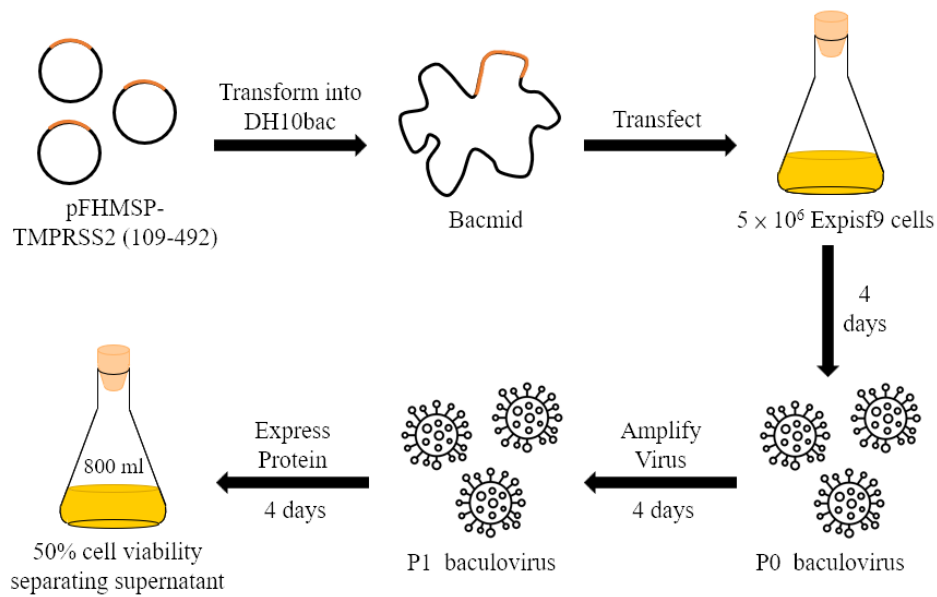


A

 Low-Density Lipoprotein Receptor (LDLR) domain

 Scavenger Receptor Cysteine-Rich (SRCR) domain

 Trypsin-like Serine Protease (SP) domain

B

C

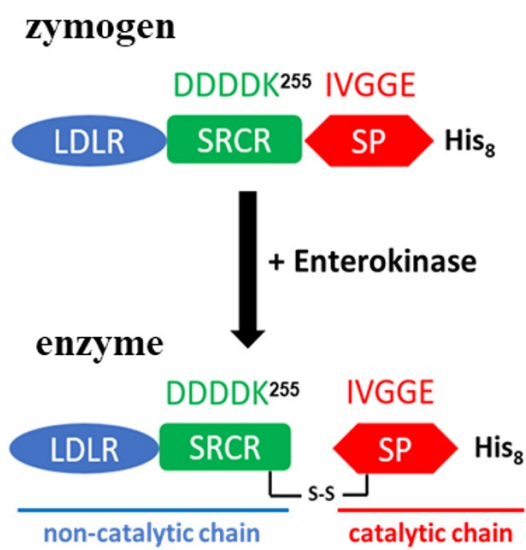
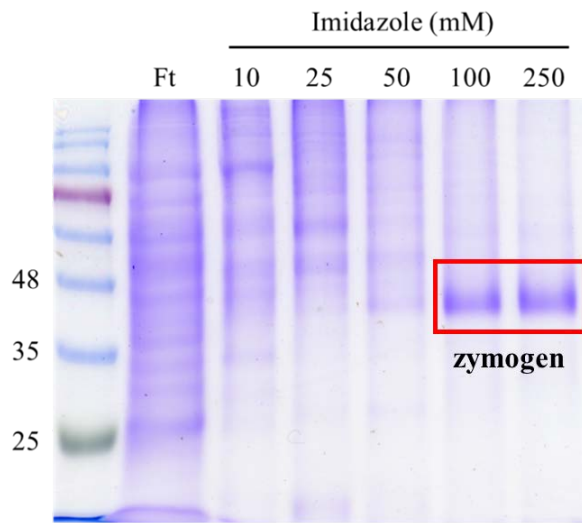


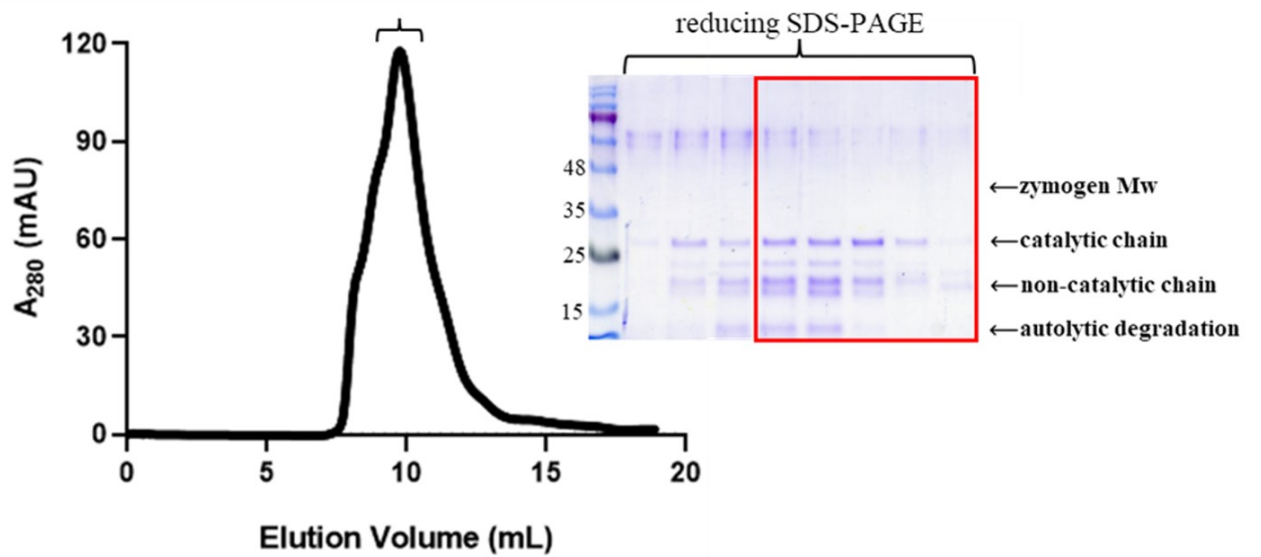
Figure 2. The subdomains of TMPRSS2 ectodomain and the strategy for the expression of TMPRSS2 ectodomain. (A) The subdomains of TMPRSS2 ectodomain, including a low-density lipoprotein receptor (LDLR) domain, a scavenger receptor cysteine-rich (SRCR) domain and a C-terminal trypsin-like serine protease (SP) domain with a canonical H296-D345-S441 catalytic triad. (B) The procedures for using baculovirus to infect ExpiSf9 insect cells for overproducing TMPRSS2 ectodomain. (C) The protocol for activating the expressed TMPRSS2 ectodomain using enterokinase.



A



B



C

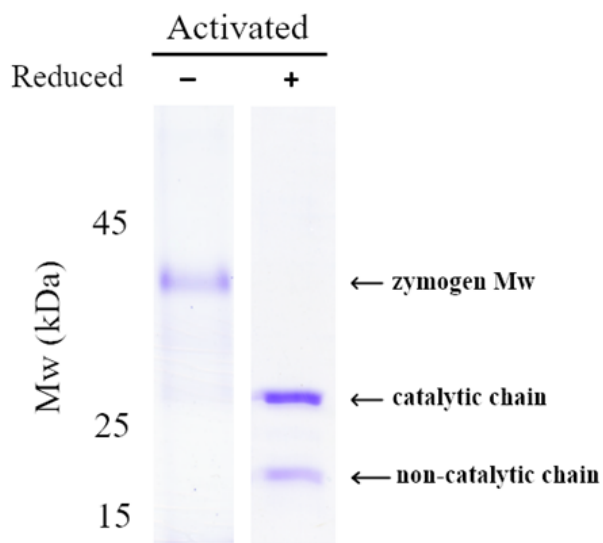
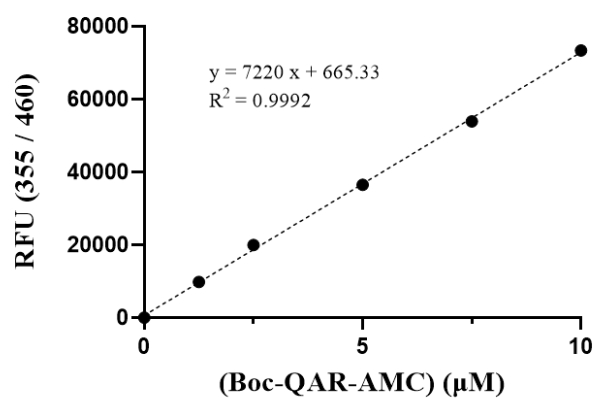


Figure 3. Purification of TMPRSS2 ectodomain. SDS-PAGE analysis of TMPRSS2 purified using (A) a Ni-NTA (HisTrap) column and subsequently passed through (B) a Superdex 75 10/300 GL column. (C) SDS-PAGE analysis of a disulfide bond formation between non-catalytic (LDLR+SRCR) and catalytic (SP) chains under non-reducing and reducing conditions.

A



B



C

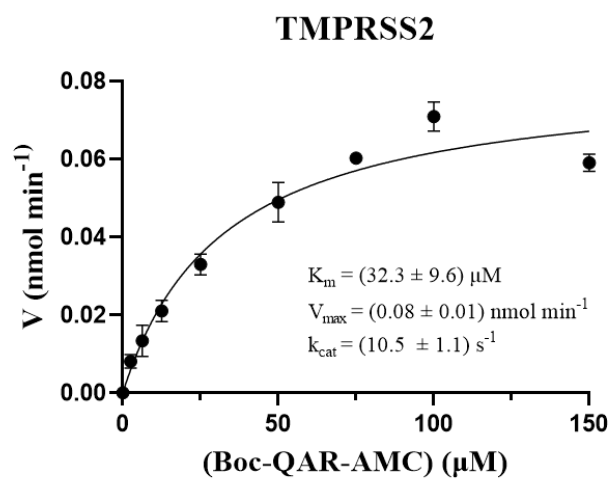
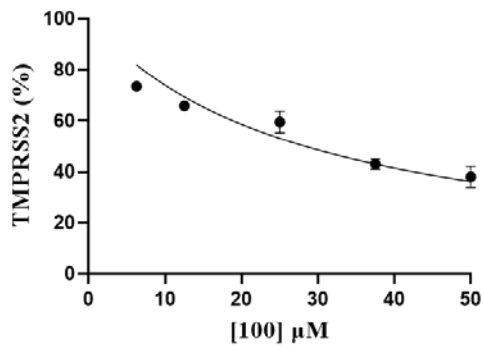
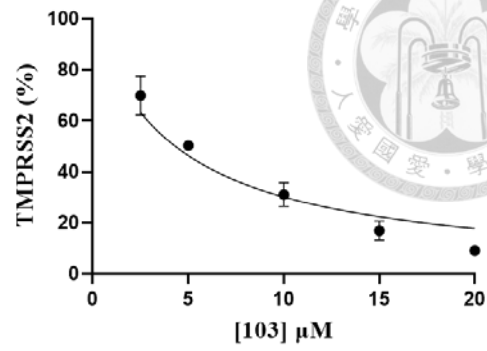
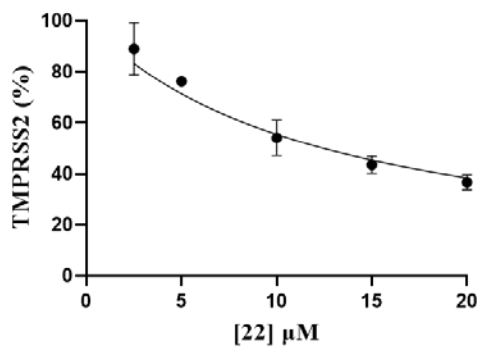
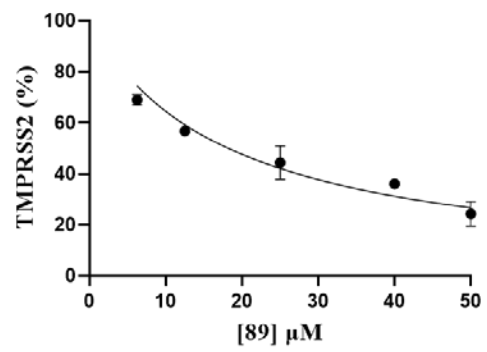
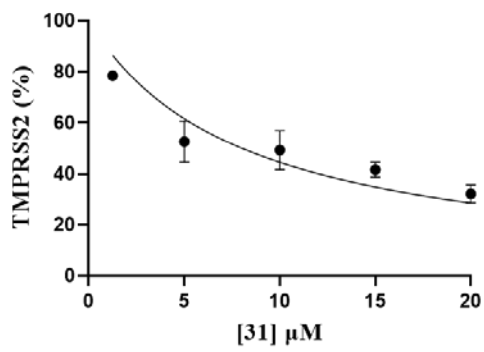
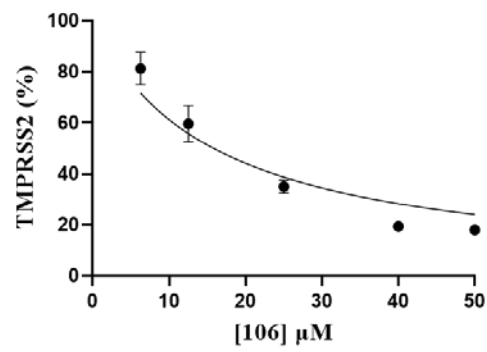
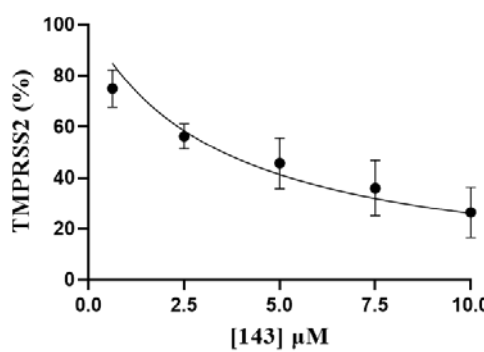
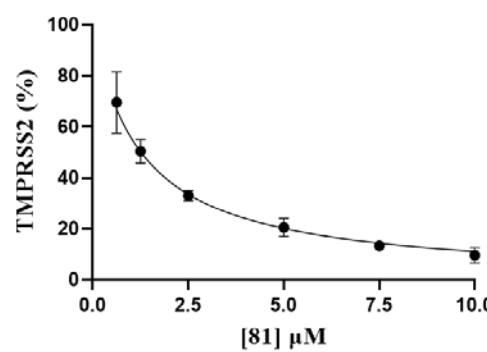


Figure 4. Characterization of the kinetic constants of the recombinant TMPRSS2 ectodomain. (A) Using the substrate Boc-QAR-AMC, the fluorescence increased due to formation of product was monitored at 460 nm by excitation at 355 nm. (B) Correlation of the fluorescence signals with the product concentrations was determined after the specified concentrations of substrate Boc-QAR-AMC were completely converted to the product. (C) The initial reaction rates of TMPRSS2 ectodomain were plotted against different substrate concentrations to yield the K_m and k_{cat} values. The obtained values are consistent with the reported numbers (Fraser et al., 2022).

A**B****C****D****E****F****G****H**

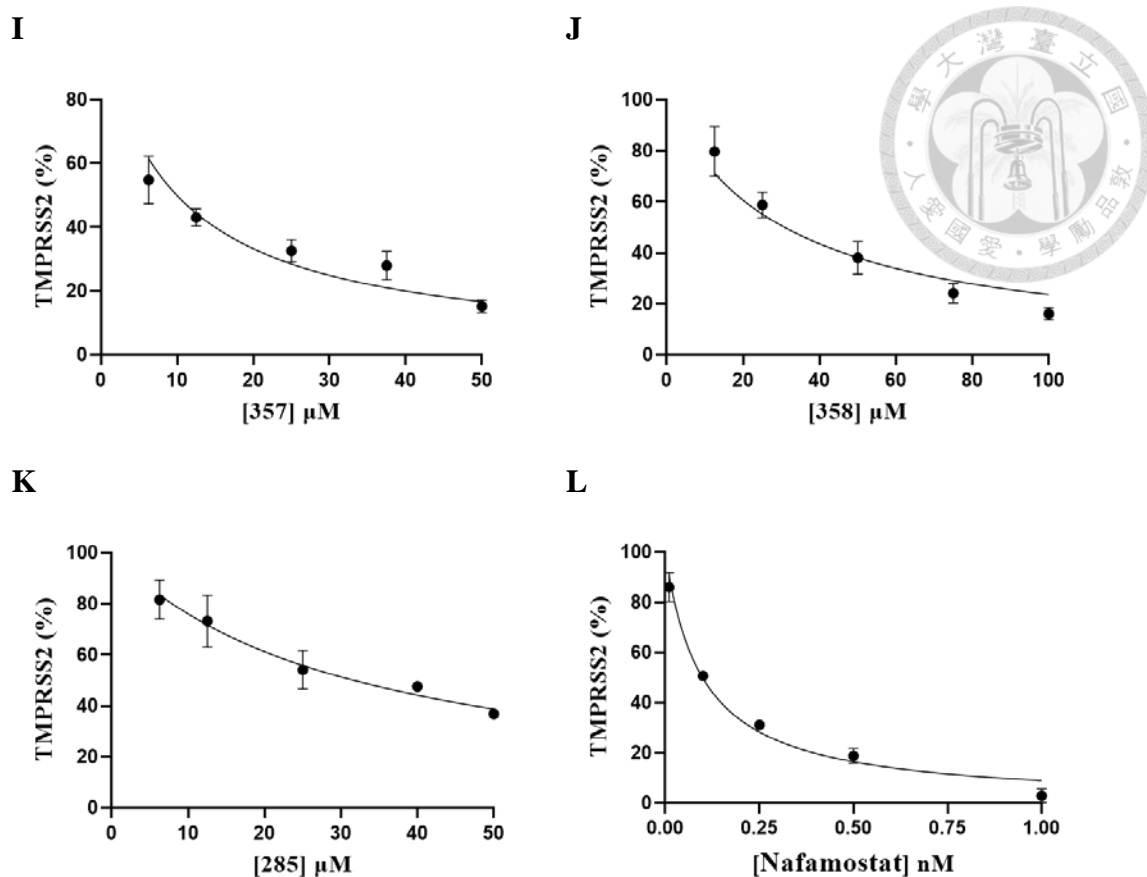
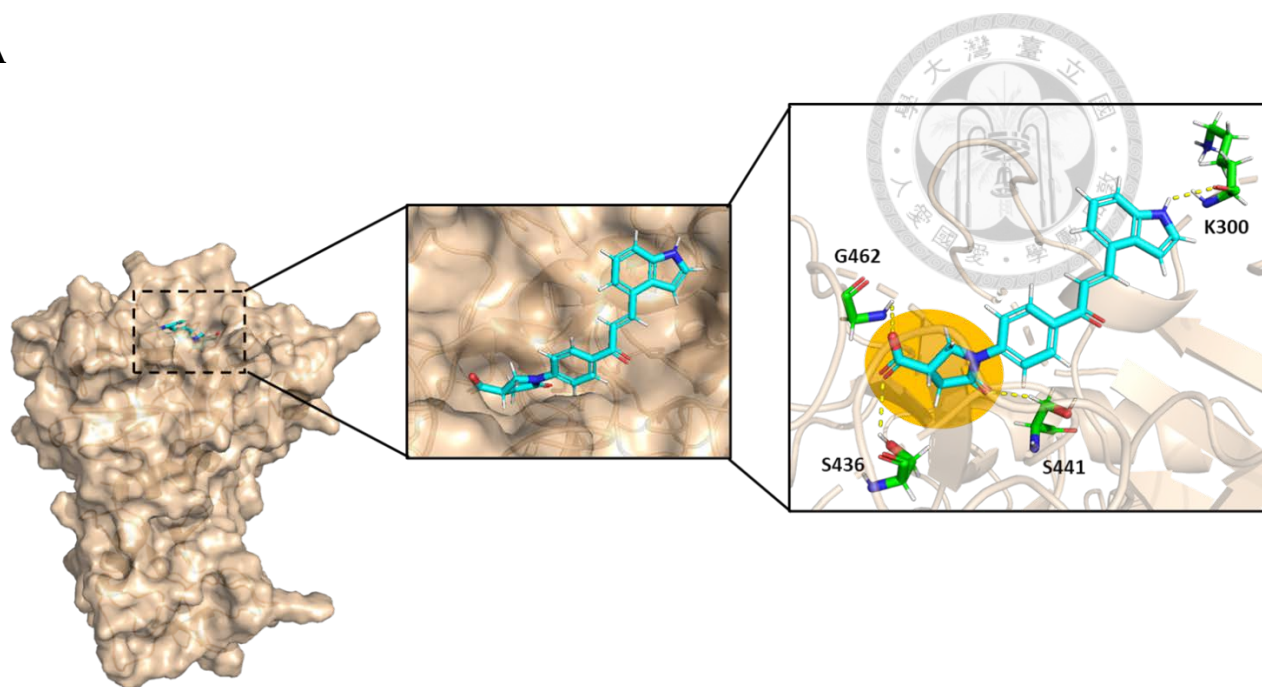


Figure 5. Inhibition of TMPRSS2 by the synthesized 4-carboxy-1-(4-styrylcarbonyl phenyl)-2-pyrrolidinones inhibitors. (A-K) The plots of inhibition percentages vs. inhibitor concentrations for IC_{50} measurements using different inhibitors. The IC_{50} of compound **81**, **143**, **103**, **22**, **31**, **106**, **100**, **89**, **357**, **358** and **285** were measured to be 1.27 ± 0.08 , 3.52 ± 0.55 , 4.32 ± 0.40 , 12.46 ± 0.95 , 8.02 ± 1.00 , 15.81 ± 1.78 , 28.35 ± 2.46 , 18.20 ± 1.45 , 9.99 ± 0.98 , 30.84 ± 3.12 and 31.64 ± 2.93 μM , respectively, based on the plots. (L) Nafamostat (positive control) displayed IC_{50} of 0.10 ± 0.01 nM.

A



B

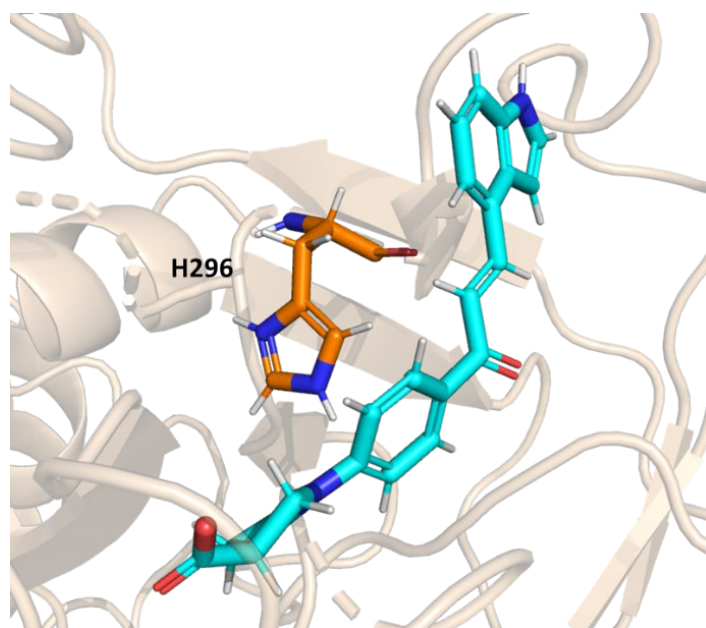
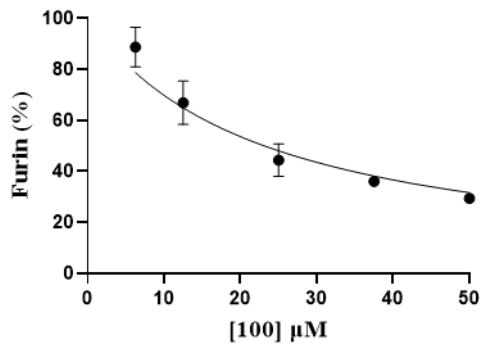
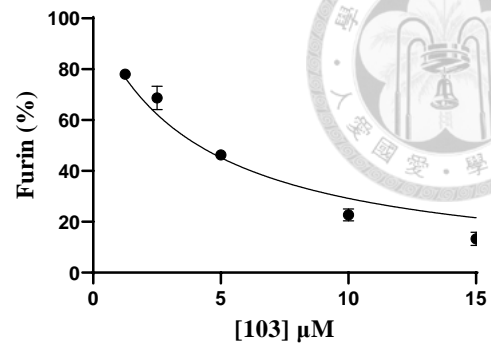
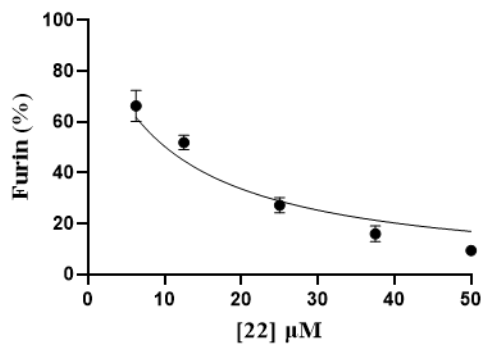
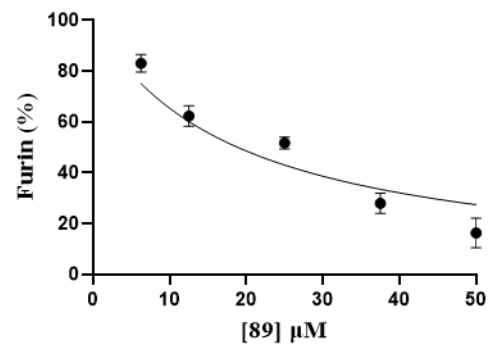
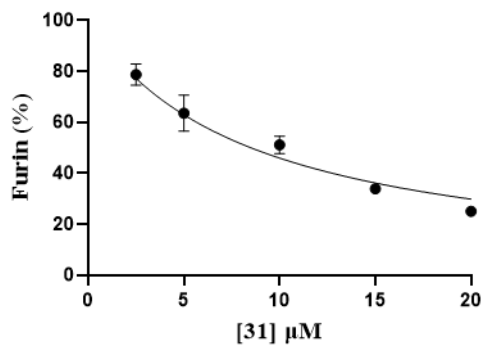
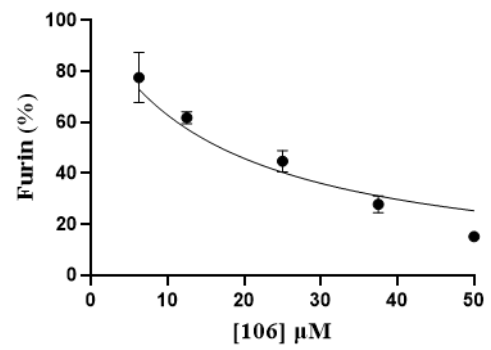
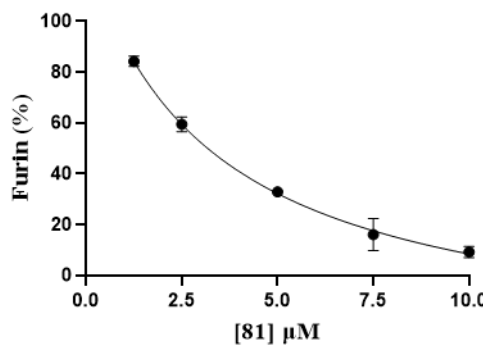
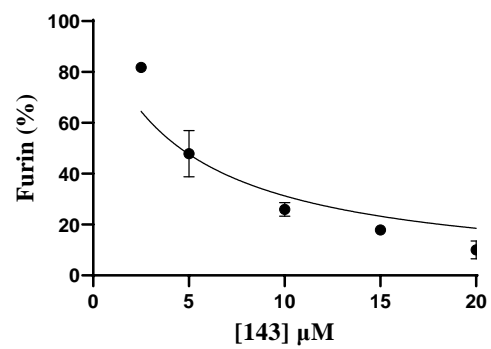
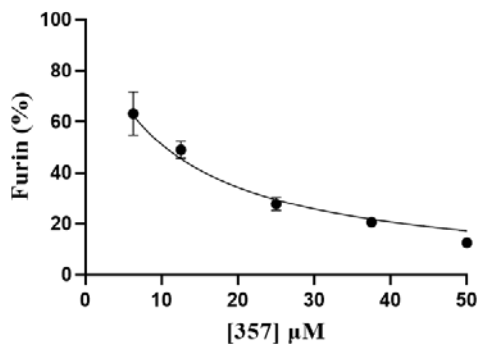


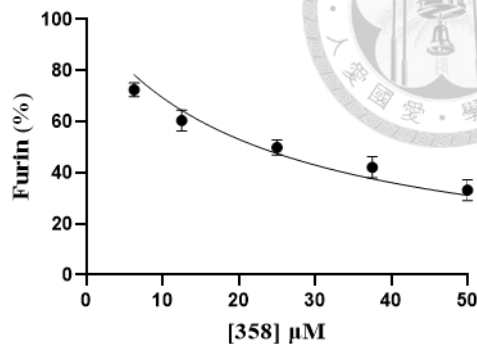
Figure 6. Modeled binding modes of the synthesized pyrrolidinone inhibitor **81** on TMPRSS2 (PDB: 7MEQ). (A) Residues colored in green were involved in hydrogen bonding interactions. (B) H296, one of TMPRSS2 catalytic triad, exhibited a charge interaction with the benzene ring of **81**.

A**B****C****D****E****F****G****H**

I



J



K

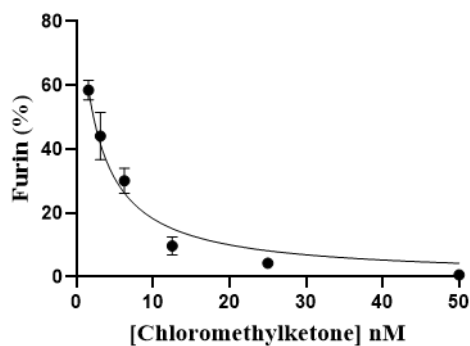
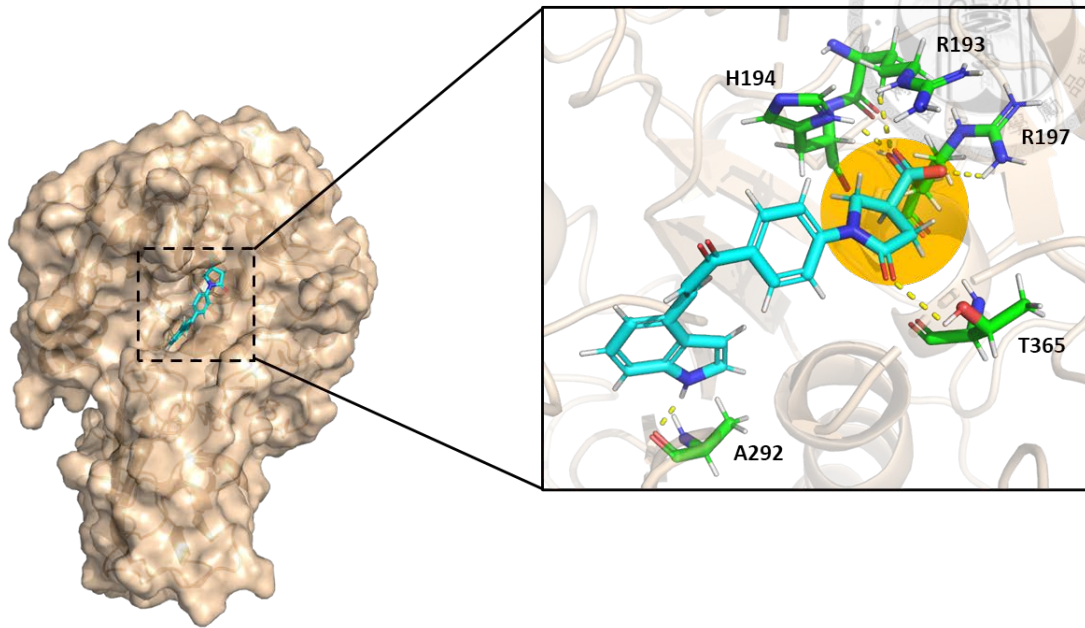


Figure 7. Inhibition of Furin by the synthesized 4-carboxy-1-(4-styrylcarbonylphenyl)-2-pyrrolidinones inhibitors. (A-J) The plots of inhibition percentages vs. inhibitor concentrations with respect to different inhibitors for IC_{50} measurements. The IC_{50} of compound **81**, **143**, **103**, **31**, **89**, **22**, **100**, **106**, **357** and **358** were measured to be 3.31 ± 0.52 , 4.55 ± 0.69 , 4.13 ± 0.41 , 8.50 ± 0.57 , 18.89 ± 2.30 , 10.14 ± 1.12 , 23.12 ± 2.35 , 16.91 ± 1.83 , 10.45 ± 0.67 and $22.66 \pm 1.63 \mu\text{M}$, respectively, based on the plots. (K) Chloromethylketone (positive control) displayed IC_{50} of $2.23 \pm 0.17 \text{ nM}$.

A



B

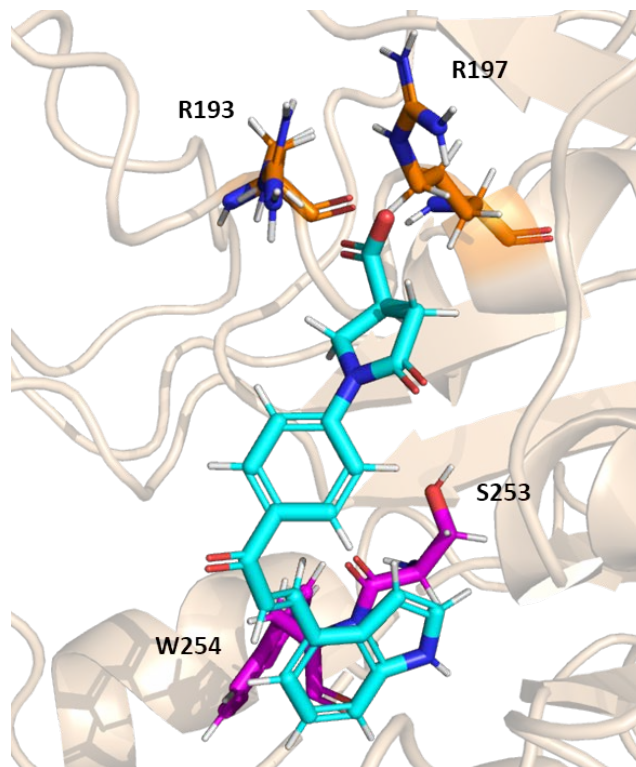


Figure 8. Modeled binding modes of the synthesized pyrrolidinone inhibitor **81** on Furin (PDB: 4RYD). Residues colored in green, orange and magenta were involved in (A) hydrogen bonding interactions, (B) charge interactions and hydrophobic interactions, respectively.



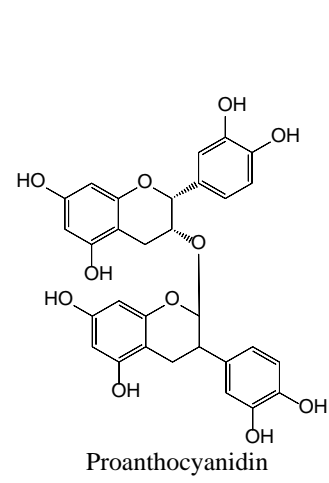
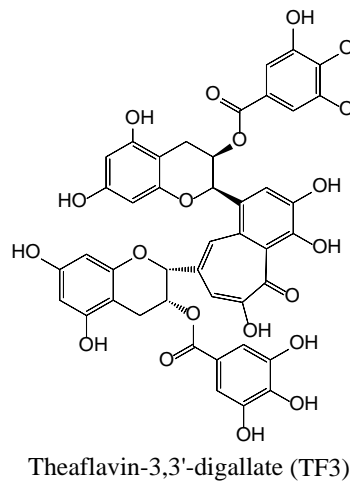
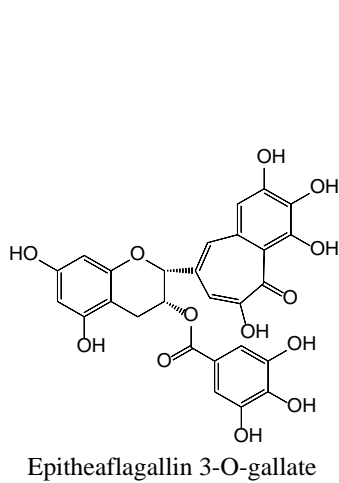
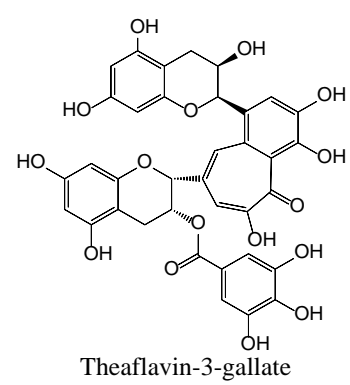
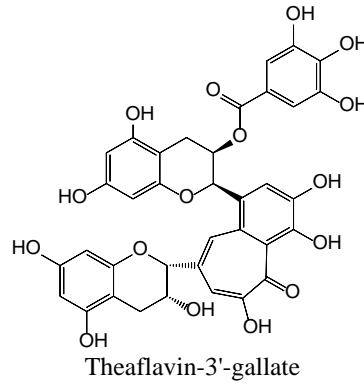
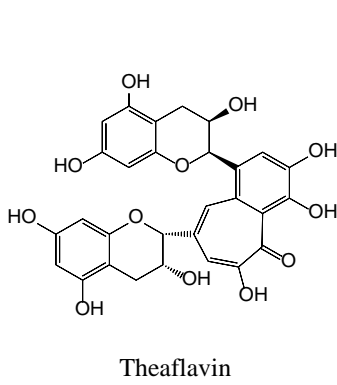
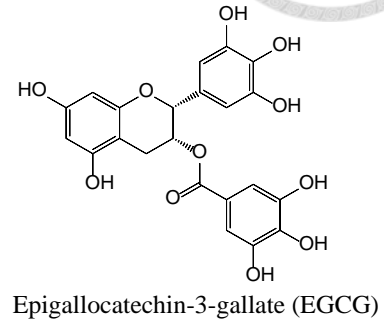
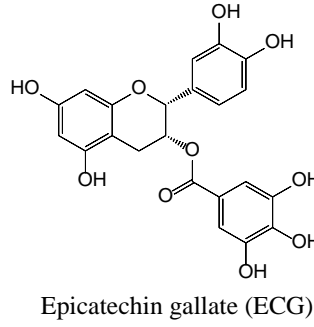
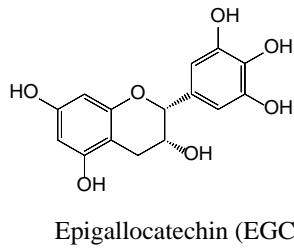
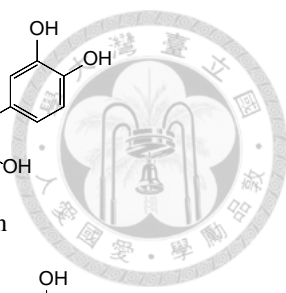
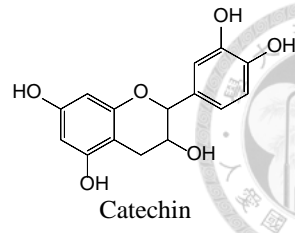
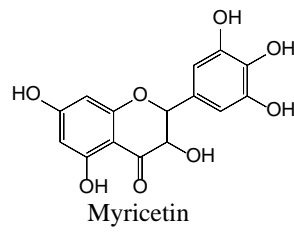
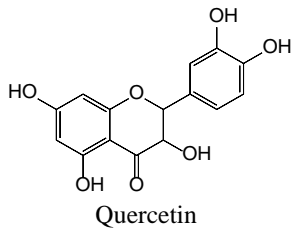
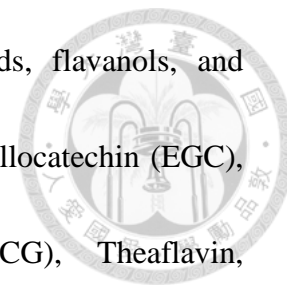


Figure 9. The chemical structures of some selected flavonoids, flavanols, and polyphenols. These include Quercetin, Myricetin, Catechin, Epigallocatechin (EGC), Epicatechin gallate (ECG), Epigallocatechin-3-gallate (EGCG), Theaflavin, Theaflavin-3-gallate, Theaflavin-3'-gallate, Epitheafllagallin 3-O-gallate, Theaflavin-3,3'-digallate (TF3), and Proanthocyanidin. The structures are arranged from smaller molecules in the top-left to larger ones in the bottom-right.



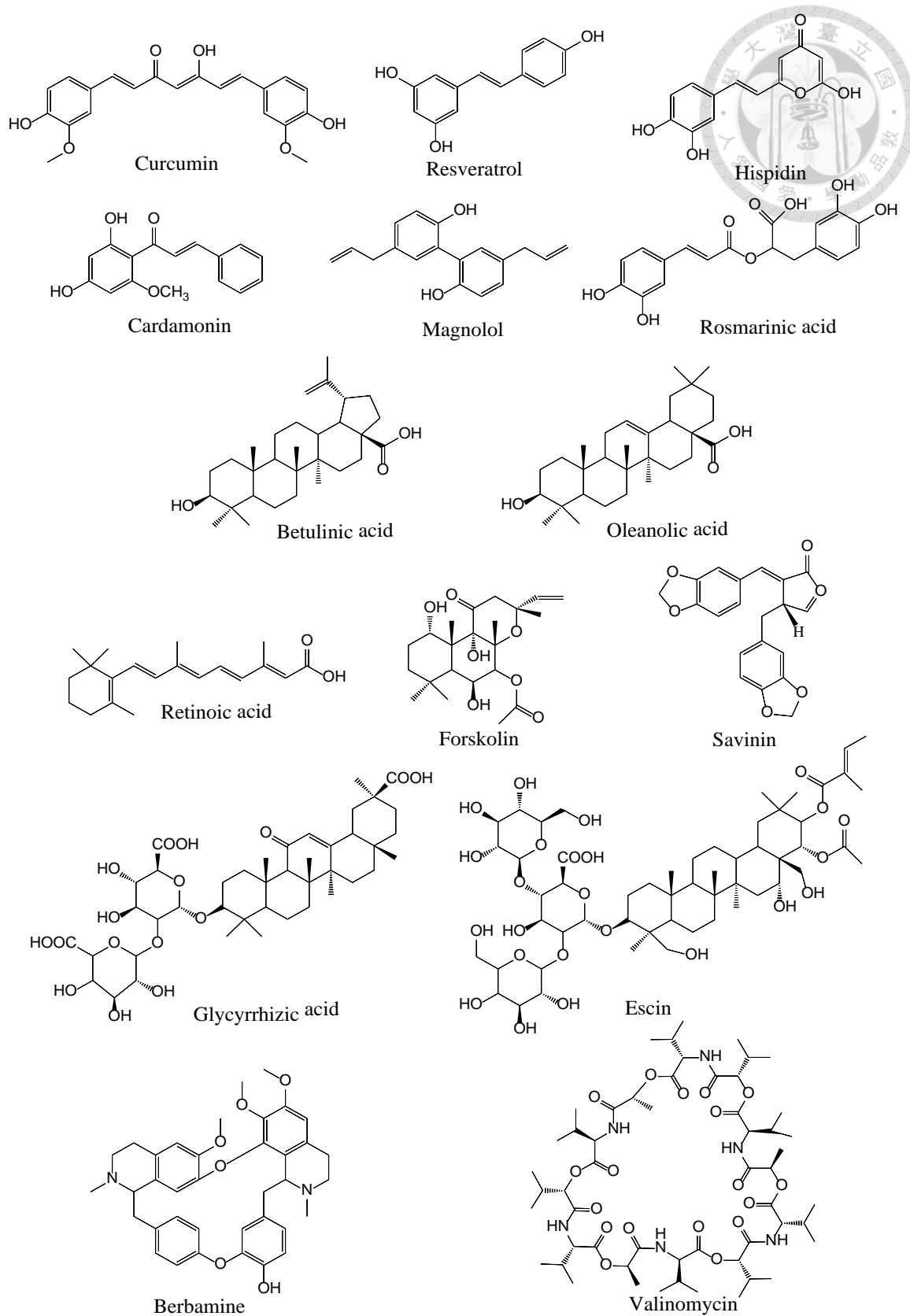
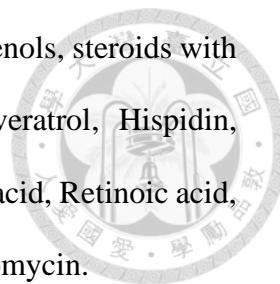


Figure 10. The chemical structures of some selected unsaturated phenols, steroids with or without sugar moieties, etc. These include Curcumin, Resveratrol, Hispidin, Cardamonin, Magnolol, Rosmarinic acid, Betulinic acid, Oleanolic acid, Retinoic acid, Forskolin, Savinin, Glycyrrhizic acid, Escin, Berbamine, and Valinomycin.



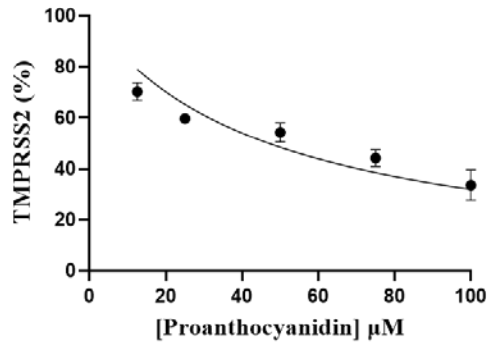


Figure 11. Testing the inhibition of TMPRSS2, Furin, and/or Cathepsin L using the 6 FDA-approved drugs previously been shown to inhibit 3CL^{pro} and/or PL^{pro}, as well as antivirals. Only Proanthocyanidin was an effective TMPRSS2 inhibitor. The plot of inhibition percentages vs. inhibitor concentrations with respect to Proanthocyanidin gave IC₅₀ of 47.01 ± 4.62 μM . None of the drugs were Furin or Cathepsin L inhibitor.

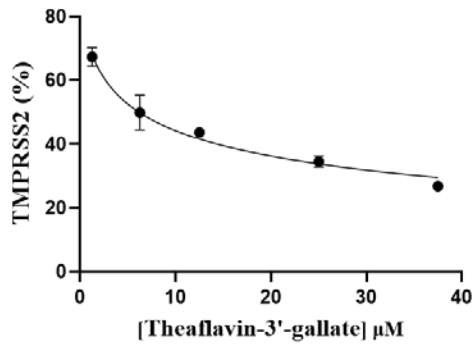
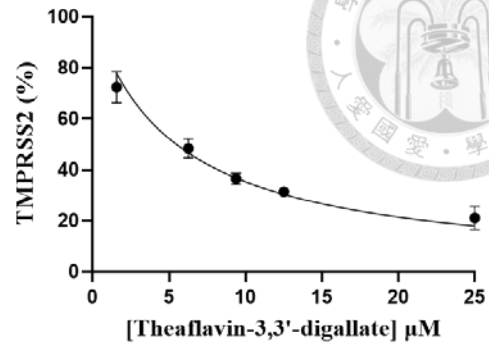
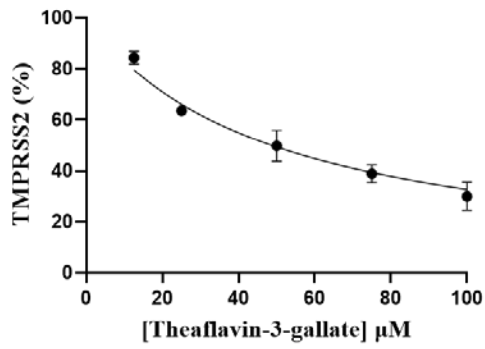
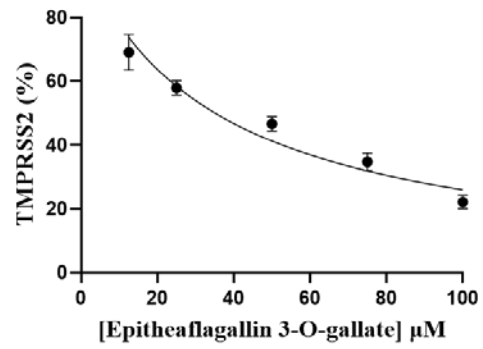
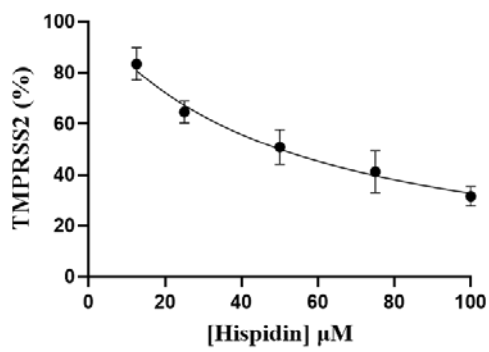
A**B****C****D****E**

Figure 12. Inhibition of TMPRSS2 by the selected natural products. Based on the plots, the IC_{50} of (A) Theaflavin-3'-gallate, (B) TF3, (C) Theaflavin-3-gallate and (D) Epitheaflagallin 3-O-gallate were measured to be 6.21 ± 0.64 , 5.47 ± 0.41 , 48.74 ± 3.02 and $35.28 \pm 2.66 \mu\text{M}$, respectively. (E) The IC_{50} of Hispidin was measured to be $50.11 \pm 3.71 \mu\text{M}$, based on the plot.

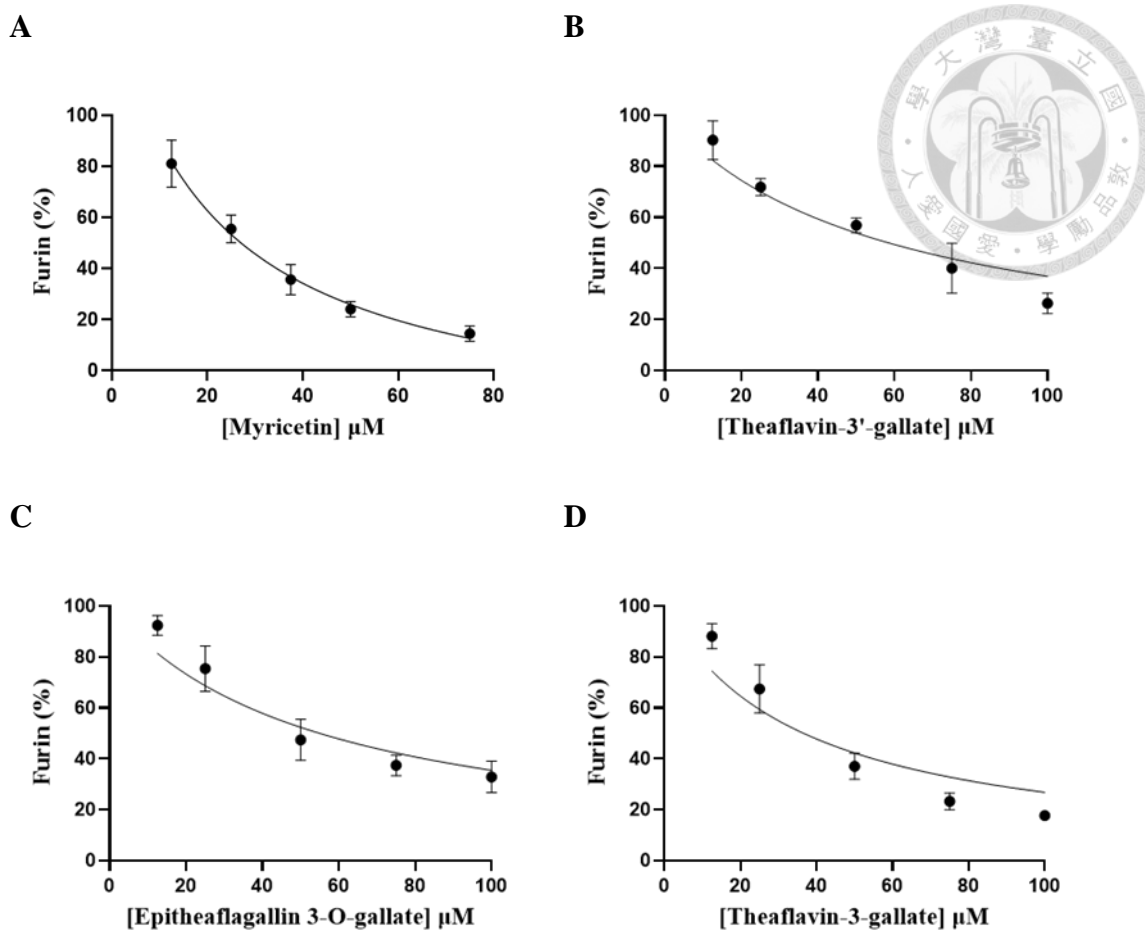


Figure 13. Inhibition of Furin by the selected natural products. Based on the plots, the IC_{50} of (A) Myricetin, (B) Theaflavin-3'-gallate, (C) Epitheaflagallin 3-O-gallate and (D) Theaflavin-3-gallate were measured to be 24.08 ± 3.52 , 58.47 ± 6.41 , 55.04 ± 6.46 and 36.67 ± 5.66 μM , respectively.

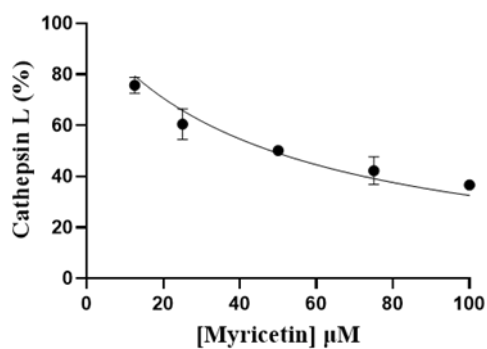
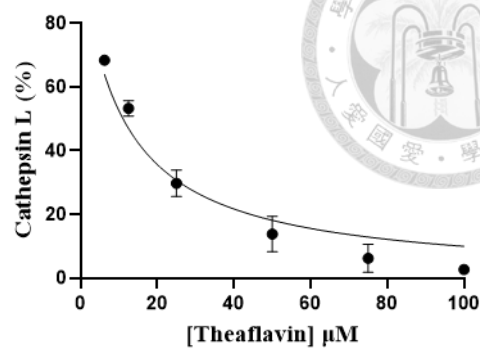
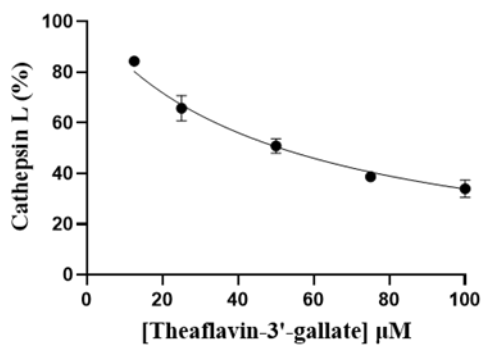
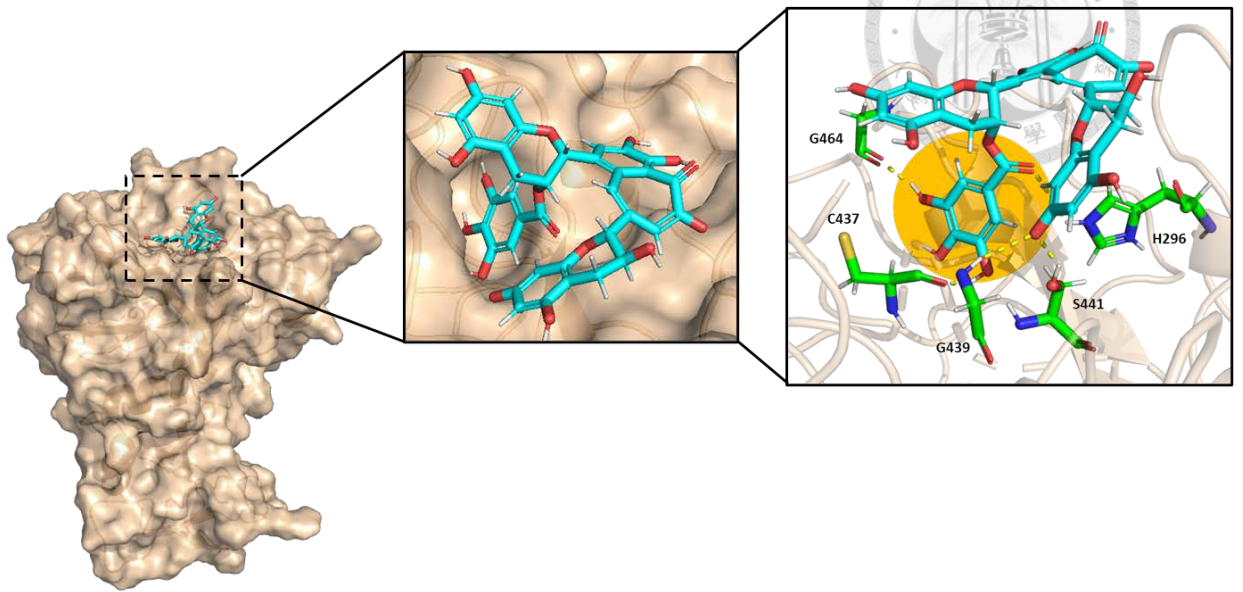
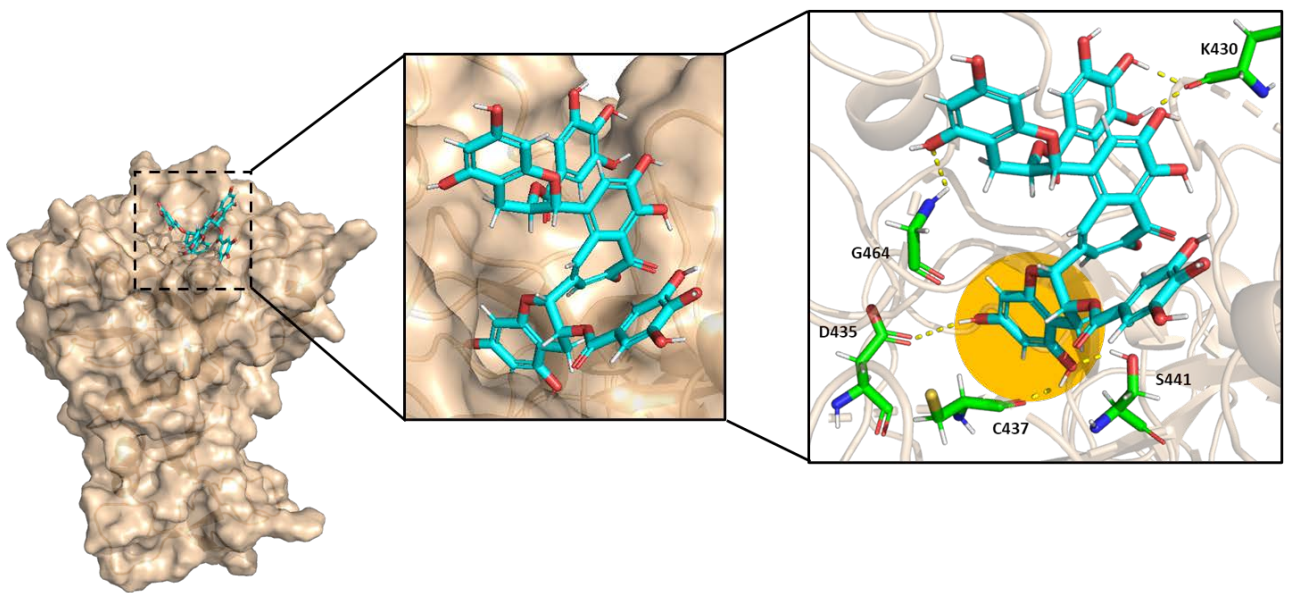
A**B****C**

Figure 14. Inhibition of Cathepsin L by the selected natural products. Based on the plot, the IC_{50} of (A) Myricetin, (B) Theaflavin and (C) Theaflavin-3'-gallate were measured to be 48.21 ± 3.57 , 11.10 ± 1.14 and 51.14 ± 2.24 μM , respectively.

A



B



C

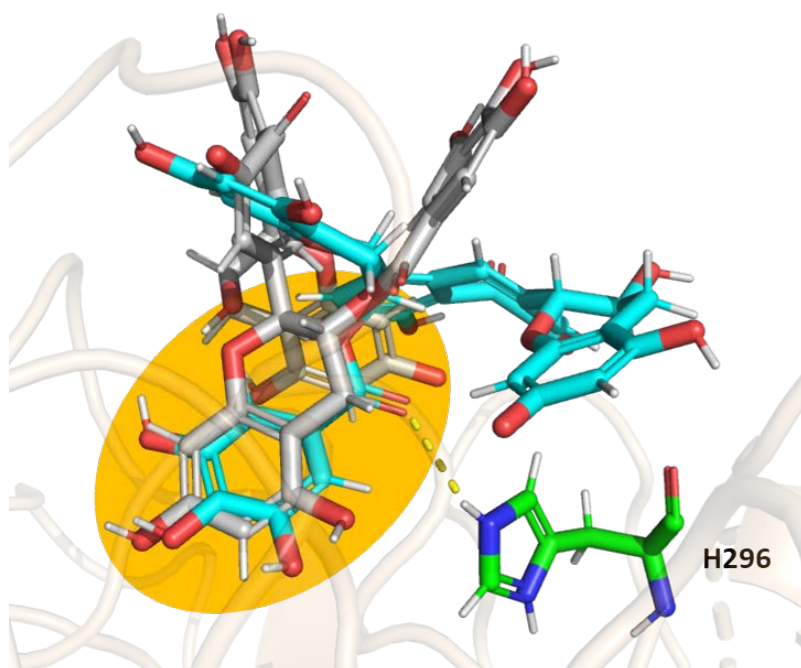
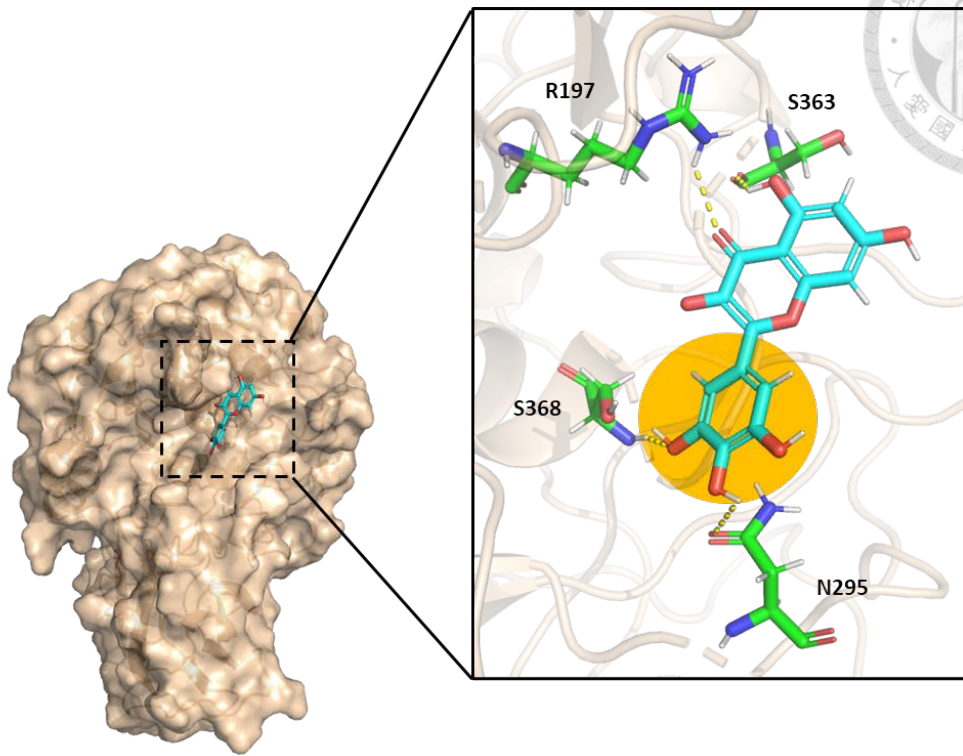
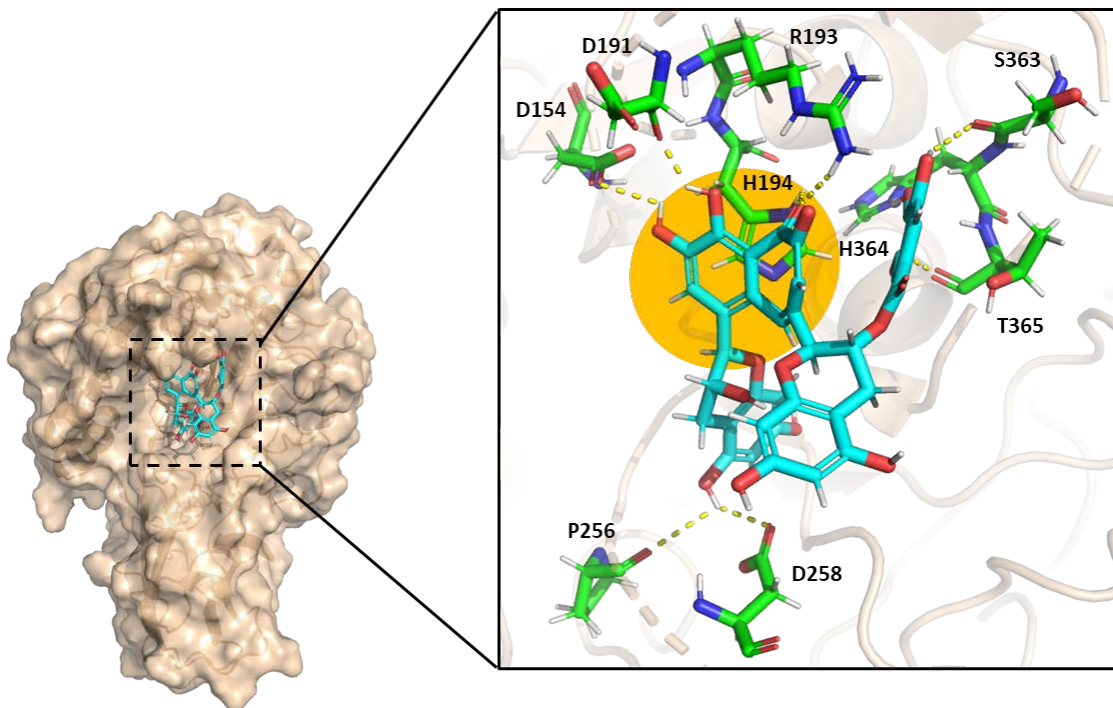


Figure 15. Modeled binding modes of the selected natural products with TMPRSS2 to rationalize their inhibition specificity. The binding modes of (A) Theaflavin-3'-gallate and (B) TF3 with TMPRSS2 (PDB: 7MEQ), respectively. (C) Comparison of the binding modes between Theaflavin-3'-gallate (cyan) and Theaflavin-3-gallate (gray).

A



B



C

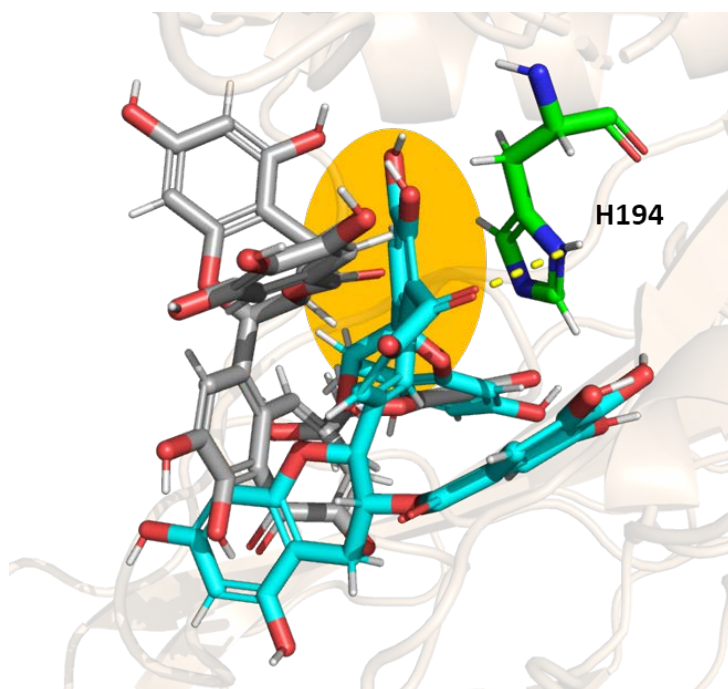
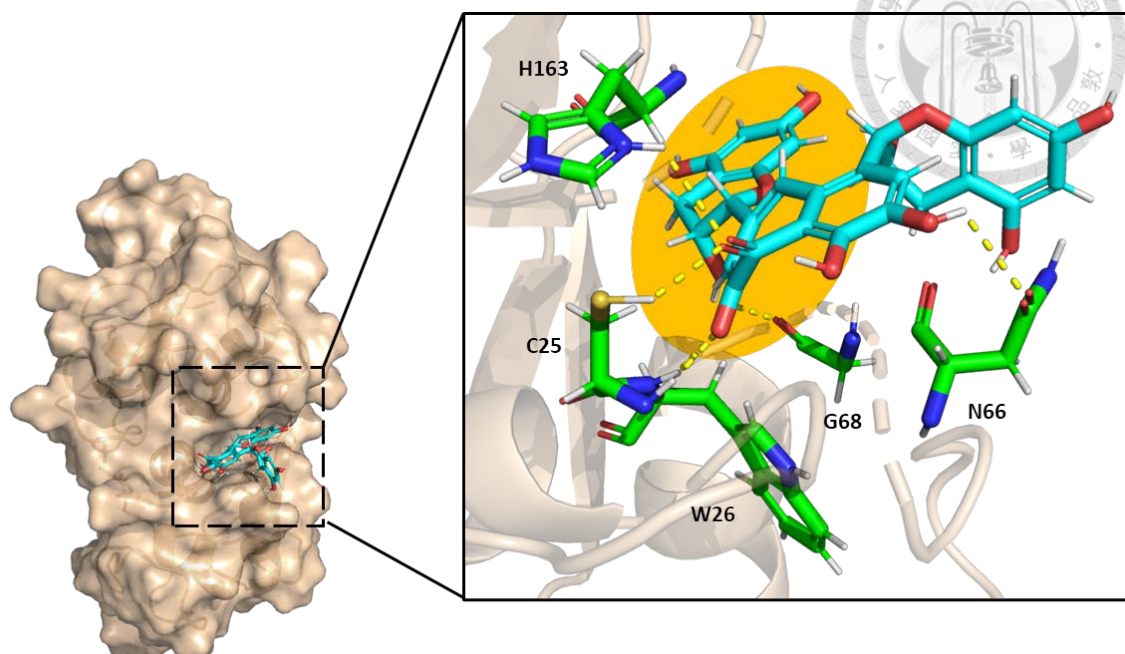


Figure 16. Modeled binding modes of the selected natural products with Furin to rationalize their inhibition specificity. The binding modes of (A) Myricetin and (B) Theaflavin-3-gallate with Furin (PDB: 4RYD), respectively. (C) Comparison of the binding modes between Theaflavin-3-gallate (cyan) and Theaflavin-3'-gallate (gray).

A



B

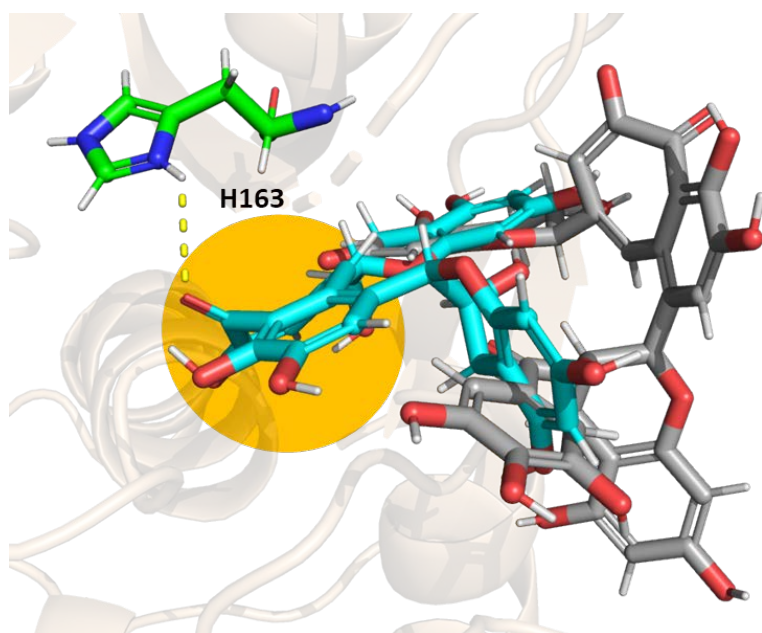
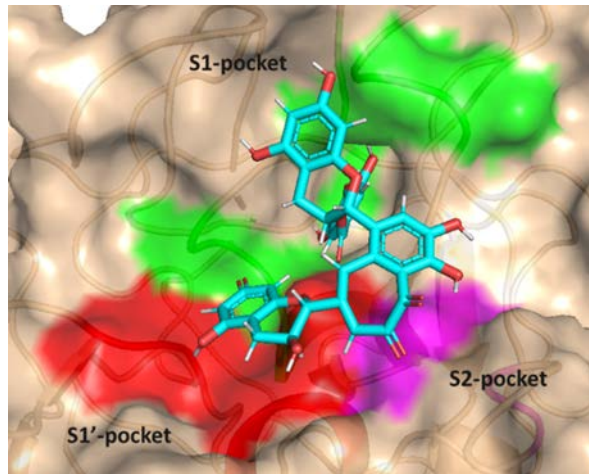


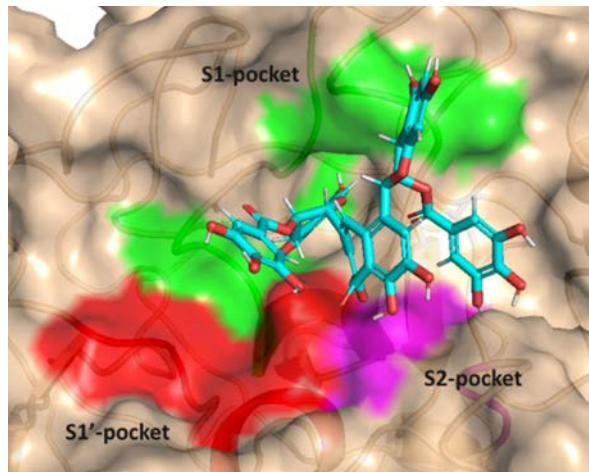
Figure 17. Modeled binding modes of the selected natural products with Cathepsin L to rationalize their inhibition specificity. The binding mode of (A) Theaflavin with Cathepsin L (PDB: 5MQY). (B) Comparison of the binding modes between Theaflavin (cyan) and Theaflavin-3'-gallate (gray).



A



B



C

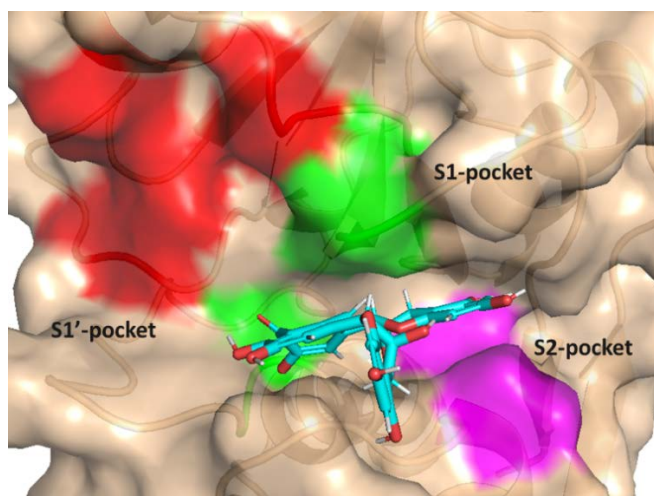
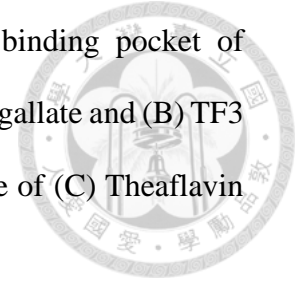


Figure 18. Analysis of the best inhibitors interacting with the binding pocket of TMPRSS2 or Cathepsin L. The binding modes of (A) Theaflavin-3'-gallate and (B) TF3 with TMPRSS2 (PDB: 7MEQ), respectively, and the binding mode of (C) Theaflavin with Cathepsin L (PDB: 5MQY).





7. Reference

Bestle D, Heindl MR, Limburg H, Van Lam van T, Pilgram O, Moulton H, Stein DA,

Hardes K, Eickmann M, Dolnik O, Rohde C, Klenk HD, Garten W, Steinmetzer T,

Böttcher-Friebertshäuser E. 2020. TMPRSS2 and furin are both essential for proteolytic activation of SARS-CoV-2 in human airway cells. *Life Sci Alliance*. 3, e202000786.

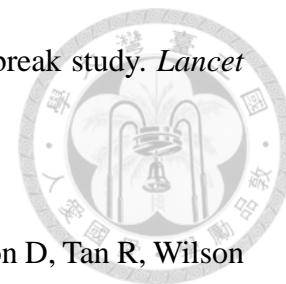
Butler, D. 2012. Clusters of coronavirus cases put scientists on alert. *Nature* 492, 166–167.

Chen CN, Lin CP, Huang KK, Chen WC, Hsieh HP, Liang PH, Hsu JT. 2005. Inhibition of SARS-CoV 3C-like Protease Activity by Theaflavin-3,3'-digallate (TF3). *Evid Based Complement Alternat Med* 2, 209–215.

Chen YW, Lee MS, Lucht A, Chou FP, Huang W, Havighurst TC, Kim K, Wang JK, Antalis TM, Johnson MD, Lin CY. 2010. TMPRSS2, a serine protease expressed in the prostate on the apical surface of luminal epithelial cells and released into semen in prostatesomes, is misregulated in prostate cancer cells. *Am. J. Pathol.* 176, 2986–2996.

Cho SY, Kang JM, Ha YE, Park GE, Lee JY, Ko JH, Lee JY, Kim JM, Kang CI, Jo IJ, Ryu JG, Choi JR, Kim S, Huh HJ, Ki CS, Kang ES, Peck KR, Dhong HJ, Song JH, Chung DR, Kim YJ. 2016. MERS-CoV outbreak following a single patient exposure

in an emergency room in South Korea: An epidemiological outbreak study. *Lancet* 388, 994–1001.



Fraser BJ, Beldar S, Seitova A, Hutchinson A, Mannar D, Li Y, Kwon D, Tan R, Wilson

RP, Leopold K, Subramaniam S, Halabelian L, Arrowsmith CH, Bénard F. 2022.

Structure and activity of human TMPRSS2 protease implicated in SARS-CoV-2 activation. *Nature Chem. Biol.* 18, 963–971.

Goc A, Sumera W, Rath M, Niedzwiecki A. 2021. Phenolic compounds disrupt spike-mediated receptor-binding and entry of SARS-CoV-2 pseudo-virions. *PLoS One* 16, e0253489.

Hoffmann M, Schroeder S, Kleine-Weber H, Müller MA, Drosten C, Pöhlmann S. Nafamostat mesylate blocks activation of SARS-CoV-2: 2020. New treatment option for COVID-19. *Antimicrob Agents Chemother.* 64, e00754-20.

Hoffman RL, Kania RS, Brothers MA, Davies JF, Ferre RA, Gajiwala KS, He M, Hogan RJ, Kozminski K, Li LY, Lockner JW, Lou J, Marra MT, Mitchell LJ Jr, Murray BW, Nieman JA, Noell S, Planken SP, Rowe T, Ryan K, Smith GJ 3rd, Solowiej JE, Stepan CM, Taggart B. 2020. Discovery of ketone-based covalent inhibitors of Coronavirus 3CL proteases for the potential therapeutic treatment of COVID-19. *J Med Chem.* 63, 12725–12747.

Huang C, Wang Y, Li X, Ren L, Zhao J, Hu Y, Zhang L, Fan G, Xu J, Gu X, Cheng Z, Yu T, Xia J, Wei Y, Wu W, Xie X, Yin W, Li H, Liu M, Xiao Y, Gao H, Guo L, Xie J, Wang G, Jiang R, Gao Z, Jin Q, Wang J, Cao B. 2020. Clinical features of patients infected with 2019 novel coronavirus in Wuhan, China. *Lancet* 395, 497–506.

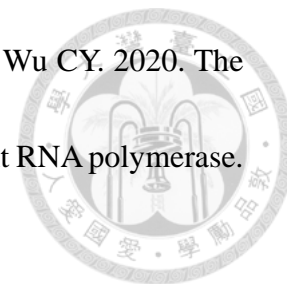
Jang M, Park YI, Cha YE, Park R, Namkoong S, Lee JI, Park J. 2020. Tea polyphenols EGCG and theaflavin inhibit the activity of SARS-CoV-2 3CL-protease in vitro. *Evid Based Complement Alternat Med* 5630838.

Jantan I, Arshad L, Septama AW, Haque MA, Mohamed-Hussein ZA, Govender NT. 2022. Antiviral effects of phytochemicals against severe acute respiratory syndrome coronavirus 2 and their mechanisms of action: A review. *Phytother Res*. 10.1002/ptr.7671.

Ksiazek TG, Erdman D, Goldsmith CS, Zaki SR, Peret T, Emery S, Tong S, Urbani C, Comer JA, Lim W, Rollin PE, Dowell SF, Ling AE, Humphrey CD, Shieh WJ, Guarner J, Paddock CD, Rota P, Fields B, DeRisi J, Yang JY, Cox N, Hughes JM, LeDuc JW, Bellini WJ, Anderson LJ, SARS Working Group. 2003. A novel coronavirus associated with severe acute respiratory syndrome. *N Eng J Med* 348, 1953–1966.

Lung J, Lin YS, Yang YH, Chou YL, Shu LH, Cheng YC, Liu HT, Wu CY. 2020. The potential chemical structure of anti-SARS-CoV-2 RNA-dependent RNA polymerase.

J Med Virol 92, 693–697.



Marín-Palma D, Tabares-Guevara JH, Zapata-Cardona MI, Flórez-Álvarez L, Yepes LM, Rugeles MT, Zapata-Builes W, Hernandez JC, Taborda NA. 2021. Curcumin inhibits in vitro SARS-CoV-2 infection in Vero E6 cells through multiple antiviral mechanisms. *Molecules* 26, 6900.

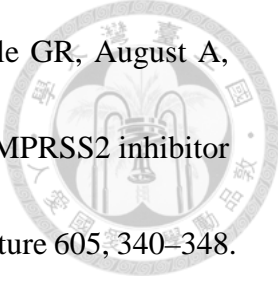
Munafò F., Donati E., Brindani N., Ottonello G., Armirotti A., De Vivo M. 2022.

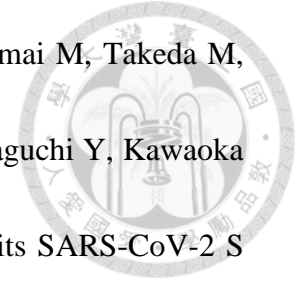
Quercetin and luteolin are single-digit micromolar inhibitors of the SARS-CoV-2 RNA-dependent RNA polymerase. *Sci. Rep.* 12, 10571.

Peiris JS, Lai ST, Poon LL, Guan Y, Yam LY, Lim W, Nicholls J, Yee WK, Yan WW, Cheung MT, Cheng VC, Chan KH, Tsang DN, Yung RW, Ng TK, Yuen KY, SARS study group. 2003. Coronavirus as a possible cause of severe acute respiratory syndrome. *Lancet* 361, 1319–1325.

Rauf A, Imran M, Abu-Izneid T, Iqbal H, Patil S, Pan X, Naz S, Sanches Silva A, Saeed F, Rasul Suleria HA. 2019. Proanthocyanidins: A comprehensive review. *Biomed Pharmacother* 116, 108999.

Shapira T, Monreal IA, Dion SP, Buchholz DW, Imbiakha B, Olmstead AD, Jager M, Désilets A, Gao G, Martins M, Vandal T, Thompson CAH, Chin A, Rees WD,

- 
- Steiner T, Nabi IR, Marsault E, Sahler J, Diel DG, Van de Walle GR, August A, Whittaker GR, Boudreault PL, Leduc R, Aguilar HC, Jean F. A TMPRSS2 inhibitor acts as a pan-SARS-CoV-2 prophylactic and therapeutic. 2022. *Nature* 605, 340–348.
- Wang SC, Chen Y, Wang YC, Wang WJ, Yang CS, Tsai CL, Hou MH, Chen HF, Shen YC, Hung MC. 2020. Tannic acid suppresses SARS-CoV-2 as a dual inhibitor of the viral main protease and the cellular TMPRSS2 protease. *Am J Cancer Res* 10, 4538–4546.
- Wen CC, Kuo YH, Jan JT, Liang PH, Wang SY, Liu HG, Lee CK, Chang ST, Kuo CJ, Lee SS, Hou CC, Hsiao PW, Chien SC, Shyur LF, Yang NS. 2007. Specific plant terpenoids and lignoids possess potent antiviral activities against severe acute respiratory syndrome coronavirus. *J Med Chem* 50, 4087–4095.
- Wu CY, Jan JT, Ma SH, Kuo CJ, Juan HF, Cheng YS, Hsu HH, Huang HC, Wu D, Brik A, Liang FS, Liu RS, Fang JM, Chen ST, Liang PH, Wong CH. 2004. Small molecules targeting severe acute respiratory syndrome human coronavirus. *Proc Natl Acad Sci USA* 101, 10012–10017.
- Xiao T, Cui M, Zheng C, Wang M, Sun R, Gao D, Bao J, Ren S, Yang B, Lin J, Li X, Li D, Yang C, Zhou H. 2021. Myricetin inhibits SARS-CoV-2 viral replication by targeting M(pro) and ameliorates pulmonary inflammation. *Front Pharmacol*, 12, 669642.



Yamamoto M, Kiso M, Sakai-Tagawa Y, Iwatsuki-Horimoto K, Imai M, Takeda M, Kinoshita N, Ohmagari N, Gohda J, Semba K, Matsuda Z, Kawaguchi Y, Kawaoka Y, Inoue JI. 2020. The anticoagulant nafamostat potently inhibits SARS-CoV-2 S protein-mediated fusion in a cell fusion assay system and viral infection in vitro in a cell-type-dependent manner. *Viruses* 12, 629.

Yi L., Li Z., Yuan K., Qu X., Chen J., Wang G., Zhang H., Luo H., Zhu L., Jiang P., et al. 2004. Small molecules blocking the entry of severe acute respiratory syndrome coronavirus into host cells. *J. Virol.* 78, 11334–11339.

Yu S, Zhu Y, Xu J, Yao G, Zhang P, Wang M, Zhao Y, Lin G, Chen H, Chen L, Zhang J. 2021. Glycyrrhizic acid exerts inhibitory activity against the spike protein of SARS-CoV-2. *Phytomedicine.* 85, 153364.

Zaki AM, van Boheemen S, Bestebroer TM, Osterhaus AD, Fouchier RA. 2012. Isolation of a novel coronavirus from a man with pneumonia in Saudi Arabia. *N Engl J Med* 367, 1814–1820.

Zhao MM, Yang WL, Yang FY, Zhang L, Huang WJ, Hou W, Fan CF, Jin RH, Feng YM, Wang YC, Yang JK. 2021. Cathepsin L plays a key role in SARS-CoV-2 infection in humans and humanized mice and is a promising target for new drug development. *Signal Transduct Target Ther.* 6, 134.

Zhou P, Yang XL, Wang XG, Hu B, Zhang L, Zhang W, Si HR, Zhu Y, Li B, Huang CL,
Chen HD, Chen J, Luo Y, Guo H, Jiang RD, Liu MQ, Chen Y, Shen XR, Wang X,
Zheng XS, Zhao K, Chen QJ, Deng F, Liu LL, Yan B, Zhan FX, Wang YY, Xiao GF,
Shi ZL. 2020. A pneumonia outbreak associated with a new coronavirus of probable
bat origin. *Nature* 579, 270–273.

Zhu N, Zhang D, Wang W, Li X, Yang B, Song J, Zhao X, Huang B, Shi W, Lu R, Niu
P, Zhan F, Ma X, Wang D, Xu W, Wu G, Gao GF, Tan W, China Novel Coronavirus
Investigating and Research Team. 2020. A novel coronavirus from patients with
pneumonia in China, 2019. *N Eng J Med* 382, 727–733.

DANA, Dibyendu; PATHAK, Sanjai K. A review of small molecule inhibitors and
functional probes of human cathepsin L. *Molecules*, 2020, 25.3: 698.